



universität
wien

MASTERARBEIT / MASTER'S THESIS

Titel der Masterarbeit / Title of the Master's Thesis

„Fast Programmable Control of an Optical Levitation Experiment“

verfasst von / submitted by

Gregor Meier BSc

angestrebter akademischer Grad / in partial fulfilment of the requirements for the degree of

Master of Science (MSc)

Wien, 2022 / Vienna, 2022

Studienkennzahl lt. Studienblatt /
degree programme code as it appears on
the student record sheet:

A 066 876

Studienrichtung lt. Studienblatt /
degree programme as it appears on
the student record sheet:

Master Physik
Master's degree programme Physics

Betreut von / Supervisor:

Ass. Prof. Dr. Nikolai Kiesel

Mitbetreut von / Co-Supervisor:

Mario Arnolfo Ciampini, PhD

Acknowledgements

Dear Nikolai, I'm honored to study under your supervision. Thank you for your help and support during this thesis, which by far exceeded my expectations. Thank you for your honesty and encouragement to take this step.

Dear Mario, I'm still wondering what would have happened if I didn't try everything to get into your quantum information course during my Bachelor's. Your fascination with what you do is reflected in your explanations and contagious for me to find out what you're up to. Thank you for all your efforts.

Dear Stefan, I'm grateful to have you as a labmate. Asking you for help feels like asking a friend for support. You've certainly saved me time and struggle and I appreciate your sense of solidarity.

Dear Lukas, as the architect of our experiment I have to say you meet my taste in what is cool science. Thank you for the insight you provided during our conversations.

I want to thank everyone who has in some way or another contributed to this thesis. This includes Paul, Jakob, Yuriy, Aisling, Gerard, Uros, Luca, Lorenzo, and Markus Aspelmeyer.

Furthermore, I want to say thank you to my parents for their unsurpassable support and affection throughout my life.

Johannes, I think we both agree that sound waves are also fairly satisfying (most of the time).

Lea, I'm looking forward to visiting the most magical garden on earth, taking a dip in the Ganges, and exploring the Himalayan mysteries with you this summer.

Abstract

Optical levitation of nanoparticles in high vacuum systems enables the generation of macroscopic quantum states at masses in the order of $m = 10^8$ amu and above. Pressures below 10^{-10} mBar enable collision-free times in the order of milliseconds, thus limiting environmental decoherence as a key constraint. Another important prerequisite is the ability to control optical potentials at high speed and precision.

This thesis presents and quantifies a programmable control system for the light-field protocol of such an experiment. Based on Sinara and ARTIQ (Advanced Real-Time Infrastructure for Quantum physics), it enables the design of optical pulse sequences with timing at nanosecond resolution, scalable to multiple separate modulators while keeping high synchronicity among its outputs. After studying permissible deviations of optimized parameters for an experimental implementation of the protocol, the performance of the proposed system will be discussed with dedicated measurements.

Zusammenfassung

Optische Levitation von Nanoteilchen in Hochvakuum Systemen ermöglicht die Erzeugung makroskopischer Quantenzustände für Massen im Bereich von 10^8 amu und mehr. Drücke unter 10^{-10} mBar erlauben kollisionsfreie Zeiten von Millisekunden-Dauer, was die durch die Umgebung verursachte Dekohärenz als eine wichtige Einschränkung solcher Experimente verringert. Eine andere wichtige Voraussetzung ist die hochpräzise und schnelle Kontrolle optischer Potentiale.

In dieser These wird ein programmierbares Kontrollsystem für das Lichtfeld-Protokoll eines solchen Experiments präsentiert und quantifiziert. Aufbauend auf Sinara und ARTIQ (Advanced Real-Time Infrastructure for Quantum physics - Moderne Echtzeit Infrastruktur für Quantenphysik), ermöglicht das System das Design von Puls Se-

quenzen mit einer Auflösung von Nanosekunden und ist hochsynchron erweiterbar auf mehrere separate optische Modulatoren. Nachdem die erlaubten Abweichungen von optimierten Zahlen für das experimentelle Protokoll ausgearbeitet wurden, wird die Leistungsfähigkeit auf Basis der zugehörigen Messungen diskutiert.

Contents

1	Preparation of a Non-Gaussian Quantum State	3
1.1	Initial Gaussian State Preparation	4
1.2	Laser Pulses in the Protocol	5
1.3	Implementation of the Pulses	9
1.3.1	Standing Wave Potential	9
1.3.2	Full Protocol	11
2	Light Field Protocol and Requirements	14
2.1	Experimental Implementation	15
2.2	Protocol Requirements	17
2.2.1	Concrete Example	17
2.2.2	Precision Requirements on the Experimental Parameters	18
3	Programmable High-Precision Control of the Light Field	25
3.1	Electro-Optic Implementation: Test Setup	26
3.2	Electronic Circuit	28
3.2.1	Signal Processing in Sinara	28
3.2.2	Signal Chain	30
3.2.3	Logic Protocol and Coding in ARTIQ	32
3.3	Measurements	33
3.3.1	Preliminary Measurements	33
3.3.2	Characterization of the Pulse Performance	38
3.3.3	Discussion of the Measurement Results	47
3.4	Conclusion and Outlook	48

List of Figures

1.1	1D Quantum Harmonic Oscillator	4
1.2	Shape of the Airy Function	7
1.3	Potential Landscapes	10
1.4	Light Field Protocol	12
2.1	Optical Setup for an Experimental Implementation	15
2.2	Beam Overlap with a Mode Matching Fiber	17
2.3	Probability Distribution	18
2.4	Pulse Properties	19
2.5	Illustration of the Light Field Benchmarks	20
2.6	Simulated Deviated Probability Distribution	24
3.1	Optical Setup for Characterizing the Light Field Control	27
3.2	Sinara Frontpanel	29
3.3	Signal Chain	30
3.4	The Pulsemaster	31
3.5	Detector Calibration	34
3.6	Power Scaling	34
3.7	π -Voltage Measurement	36
3.8	AOM Extinction Ratio Measurement	37
3.9	Distribution of the Pulse Power	39
3.10	Timing Precision	40
3.11	Separate EOM Pulses	41
3.12	Correlation of Pulse Height and Area	43
3.13	Power Monitoring	44
3.14	Pulse Area Distributions	45

3.15 Exemplary Short Pulse	46
--------------------------------------	----

List of Acronyms

ADC Analog to Digital Converter

AMU Atomic Mass Unit

AOM Acousto-Optic Modulator

ARTIQ Advanced Real-Time Infrastructure for Quantum physics

BS Beam Splitter

BP Bright Port

DAC Digital to Analog Converter

DP Dark Port **EEM** Eurocard Extension Module

EOM Electro-Optic Modulator

FPGA Field Programmable Gate Array

NA Numerical Aperture

PBS Polarizing Beam Splitter

PM fiber Polarization-Maintaining fiber

SM fiber Single-Mode fiber

UHV Ultra-High Vacuum

Sinara Modules:

Kasli FPGA-Carrier (ARTIQ Master)

Urukul DDS-Based Frequency Synthesizer

DIO-SMA Digital Input Output providing TTL-Signals

Clocker Clock Distribution Module

Fastino High-Speed DAC

IDC-SMA/IDC-BNC Adapters for Fastino

Sampler ADC

Introduction

The quest for an understanding of light dates back to the origin of science itself. Already in ancient times, natural philosophers like Aristotle and Euclid reflected on different theories of light. In the 18th century, Isaac Newton had a formative influence on the corpuscular theory of light. Due to the authority of Newton's name at the time and the precise answers it provided, backed by his principles of mechanics, it was not until a century later that an undulatory theory of light, mainly elaborated by Christiaan Huygens and Augustin Fresnel, was taken into serious consideration [1].

Another century later in 1905, Einstein with his discovery of the photoelectric effect postulated the existence of photons as quanta of light, starting the debate on a wave-particle duality [2]. As an advance of Max Planck's previous work on black-body radiation [3], this marked the start of modern quantum physics. About two decades later, Louis de Broglie picked up Einstein's idea and generalized it to all moving matter, at the time mainly focused on electrons [4, 5]. In 1928, the first experimental confirmations with Thomson's thin metal diffraction experiment and the Davisson and Germer experiment followed [6, 7]. Experiments on quantum effects of larger and larger objects proceeded, from atoms [8, 9] to complex molecules [10, 11].

An increase in mass and size of the tested objects is of interest for testing the bounds of the principles of quantum theory [12]. Levitated nanoparticles are considered a suitable platform for controlling quantum states of macroscopic objects at masses of $m = 10^8$ amu and above [14, 15, 16, 17]. Assets of optical levitation are the clean mode structure, the excellent isolation from the environment, and the spatiotemporal control of the mechanical system via the light field. This is the core of the project this thesis is contributed to: It aims at the first control of the quantum state of a nanoparticle with a non-linear potential in a well-timed protocol.

This thesis presents and characterizes a programmable control system designed for a protocol aiming to prepare a non-Gaussian quantum state via pulsed interaction with cubic and unstable potentials [18]. With this system, we can perform arbitrary pulse sequences at nanosecond timing resolution. It is scalable and modular and easily adaptable beyond the presented application and to withstand complex challenges. The underlying technology is ARTIQ (Advanced Real-Time Infrastructure for Quantum physics), a Python based control system for quantum information experiments, executed on the Sinara hardware.

In the first chapter, we introduce a recently designed protocol for the optical preparation and detection of a non-Gaussian state of a nanoparticle with mass $m \geq 10^8$ amu [18].

The second chapter provides a short description of the envisioned complete experimental implementation of the scheme and defines the relevant experimental parameters along with acceptable deviations to determine the requirements on our control system. The third chapter elaborates on the designed programmable control system for the required pulses and quantifies its performance by measurements in regards to the earlier defined benchmarks. Based on our results, we conclude that the overall approach is feasible and discuss the final steps to conclude the verification of the optical control system.

Chapter 1

Preparation of a Non-Gaussian Quantum State

Given an optically levitated and ground-state cooled nanoparticle, can we create interference fringes by letting it evolve in a non-linear potential? This question was recently answered positively [18]. As we will see, it can be achieved with a fast and precise control of optical potentials. This chapter explores the theory of the particle-light interaction for a protocol creating a detectable fringe size. To give some context, it starts with a short introduction to trapped nanoparticles as quantum harmonic oscillators and Gaussian quantum states.

1.1 Initial Gaussian State Preparation

A dielectric nanoparticle trapped in an optical potential can in general be treated as a harmonic oscillator experiencing a restoring force along its displacement axis for small displacements from the trap center [25, 26, 34]:

$$F(x) = m\omega_m^2 x \quad (1.1)$$

where m is the effective mass of the particle, ω_m the mechanical frequency of the trap (where $\omega_m^2 \propto P$, with P the optical power), and $k = m\omega_m^2$ the spring constant of the system.

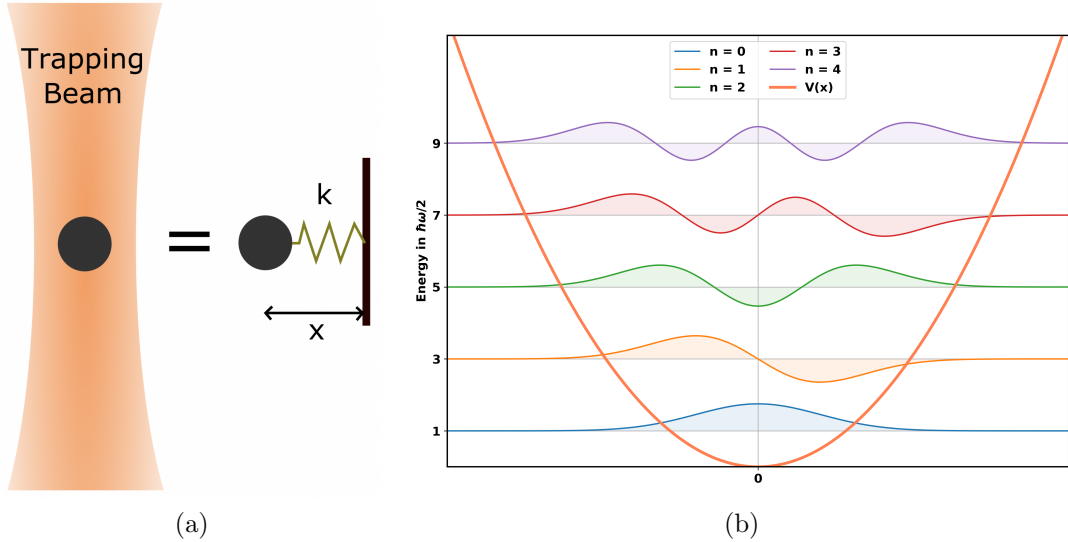


Figure 1.1: **1D Quantum Harmonic Oscillator:** a) A levitated nanoparticle can be described as a harmonic oscillator experiencing a restoring force along a displacement x with a spring constant k . b) When the particle motion is cooled towards low energy states, it can be treated as a quantum harmonic oscillator. The first few orders of solutions of the energy eigenstates ψ_n for the quantum harmonic oscillator as given in Equation 1.4 for a particle in a potential $V(x)$ with the corresponding energy levels are shown.

If the particle's motional energy is $E \sim \hbar\omega_m$, it can be treated as a quantum harmonic oscillator. In this case, the Hamiltonian of the system is given by:

$$\hat{H} = \frac{\hat{p}^2}{2m} + \frac{1}{2}k\hat{x}^2 = \frac{\hat{p}^2}{2m} + \frac{1}{2}m\omega_m^2\hat{x}^2 \quad (1.2)$$

Here the first part describes the kinetic part and the second the potential energy and \hat{x} and \hat{p} are the position and momentum operators [24]. Solving the time-independent Schrödinger equation for this Hamiltonian for a wavefunction $\psi(x) = \langle x|\psi\rangle$:

$$\hat{H} |\psi\rangle = E |\psi\rangle \quad (1.3)$$

the solutions are the Hermite functions with the Hermite polynomials $H_n(x)$:

$$\psi_n(x) = \frac{1}{\sqrt{2^n n!}} \left(\frac{m\omega_m}{\pi\hbar} \right)^{1/4} e^{-\frac{m\omega_m^2}{2\hbar} x^2} H_n \left(\sqrt{\frac{m\omega_m}{\hbar}} x \right) \quad (1.4)$$

with $E_n = \hbar\omega_m(n + 1/2)$ being the corresponding energy levels and $x_{zpf} = \sqrt{\frac{\hbar}{2m\omega_m}}$ the zero-point fluctuations of the oscillator. This is illustrated in Figure 1.1. One finds the ground-state wavefunction ψ_0 to be a Gaussian. The experimental cooling of a levitated nanoparticle to its ground-state, challenging high mass and thus a small wavefunction, has recently been achieved in three different experiments [20, 22, 23].

1.2 Laser Pulses in the Protocol

Letting a Gaussian evolve in a non-linear potential can create interference fringes in the particle wavefunction. We will show that with the necessary particle-light interactions in the form of a protocol it is possible to create detectable fringes in the particle wavefunction in position space. We divide the section into the necessary steps of the protocol: It starts with investigating the mechanics of short pulses, including a harmonic x^2 potential and a short non-linear cubic x^3 pulse for creating visible fringes in momentum space. After that, the effect of a long pulse of an inverted harmonic $-x^2$ potential for expanding the fringe spacing to a detectable size is explored.

Applying Short Laser Pulses to a Quantum Wavefunction

We start with presenting the mechanics of short laser pulses to introduce general pulse properties utilized for the protocol. We consider a pulse "short", when the time evolution in regards to the kinetic energy $\frac{p^2}{2m}$ of the particle satisfies $e^{-(i/\hbar)p^2 t/(2m)} \approx 1$ and thus $\sigma_p^2/(2m\hbar)t \ll 1$ with σ_p being the width in momentum space and t the pulse duration. In other words, the state keeps its shape in position space during the

short interaction. The kinetic part can then be neglected and the Hamiltonian can be approximated as the optical potential [19]:

$$H \approx V(x) \quad (1.5)$$

Thus the time evolution of an initial wavefunction $\Psi(x, 0)$ during such a short pulse reads:

$$\Psi(x, t) \approx e^{-\frac{i}{\hbar}V(x)t}\Psi(x, 0) \quad (1.6)$$

In order to see the time evolution in momentum space, a Fourier transform, denoted as $FT(\)$, is done on the position space wavefunction. Using the convolution theorem denoted by $*$, one finds:

$$\Psi(p, t) \approx \frac{1}{\sqrt{2\pi\hbar}} FT \left(e^{-\frac{i}{\hbar}V(x)t} \right) * \Psi(p, 0) \quad (1.7)$$

where the first part before $*$ is the momentum space propagator $K(p, t)$.

For multiple potentials applied at the same time, the initial wavefunction is convoluted with the corresponding additional propagators of each potential. Due to a convolution being commutative and associative, this is equal to doing a sequence of pulses with different potentials at different times. Thus also the order of the pulses doesn't matter. Short laser pulses are susceptible in regards to their form since e.g. the rising- and falling edges can represent a relevant part of the pulse. For a time-dependent potential $V(x, t)$ the time evolution of the initial wavefunction becomes:

$$\Psi(x, t) = e^{-\frac{i}{\hbar} \int_0^t dt' V(x, t')} \Psi(x, 0) \quad (1.8)$$

As $\int_0^t dt' V(x, t') \propto \int_0^t dt' I(t')$ is the pulse area with $I(t)$ being the time-dependent intensity of the pulse, it follows that the pulse shape doesn't matter, but only the pulse area.

Short Cubic Pulse

The fringes in the particle wavefunction are created by a short non-linear cubic pulse. Considering a non-linear cubic potential $V_3(x) = u_3x^3$, the momentum space propag-

ator results in:

$$K_3 = \frac{1}{\sqrt{2\pi\hbar}} FT \left(e^{-\frac{i}{\hbar} u_3 x^3 t} \right) = \frac{1}{p_0(t)} \text{Airy} \left[\frac{p}{p_0(t)} \right] \quad (1.9)$$

with $p_0(t) = \sqrt[3]{3\hbar^2 u_3 t}$ and $\text{Airy}[\]$ being the Airy function.

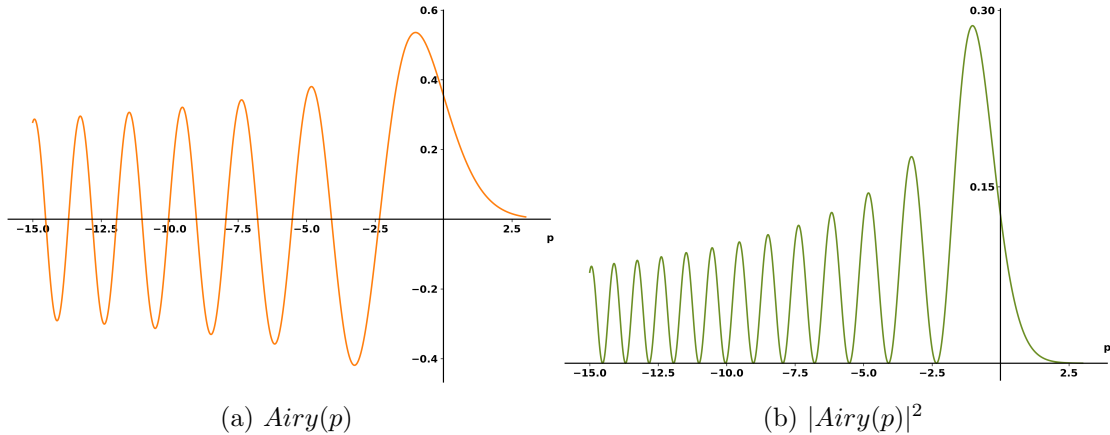


Figure 1.2: **Shape of the Airy Function:** The momentum space propagator for a short cubic pulse features an Airy function. In order to see the fringes of the Airy function in the momentum space wavefunction after convolution with the propagator, the initial momentum space uncertainty must satisfy $\sigma_p \ll \Delta p(t)$.

To calculate the momentum-space wavefunction after a cubic pulse, the propagator has to be convoluted with the wavefunction before the pulse as in Equation 1.7. Since the first two zeros of the $\text{Airy}[p]$ function are $p_1 \approx -2.33$ and $p_2 \approx -4.08$, the fringe spacing is:

$$\Delta p(t) \approx 1.75 p_0(t) \propto (\Phi)^{1/3} \quad (1.10)$$

where $\Phi = \int_0^t I(t) dt$ is the pulse area. This does not depend on the particle wavefunction but on the properties of the pulse. In the case of $\sigma_p \gg \Delta p(t)$, where the momentum space uncertainty of the initial wavefunction is much larger than the achieved fringe spacing, the fringes would get washed out. Thus it is necessary for a visible fringe spacing to prepare the initial state such that $\sigma_p \ll \Delta p(t)$.

Short Quadratic Pulse

To satisfy $\sigma_p \ll \Delta p(t)$, the wavefunction has to be prepared correspondingly. After the ground-state preparation, a free evolution of duration t_f with $V(x) = 0$ is done to increase the position uncertainty linearly in time while keeping the momentum

uncertainty constant at $p_{zpf} = \sqrt{\frac{\hbar m \omega_0}{2}}$, where ω_0 is the initial trapping and cooling frequency. This allows an increase of the initially small wavepacket size in position space. If now a quadratic pulse in the form of $V(x) = \pm u_2 x^2$ with the propagator:

$$K_{2,\pm}(p, t) = \frac{1}{\sqrt{2\pi\hbar}} FT \left(e^{\mp \frac{i}{\hbar} u_2 x^2 t} \right) = \frac{1}{\sqrt{4\pi\hbar t u_2}} e^{\pm \frac{i p^2}{4\hbar t u_2}} \quad (1.11)$$

is applied to the wavefunction after the free evolution, we obtain for $u_2 = m\omega_2^2/2$ the following condition:

$$\frac{\sigma_p^2(t)}{p_{zp}^2} = \left(1 + \mp 2\omega_2^2 t_f t + t_f^2 \omega_2^4 t_f^2 + \frac{\omega_2^2}{\omega_0^2} \omega_2^2 t \right) \quad (1.12)$$

This shows that an inverted potential leads to an increase of σ_p independent of t , while a short harmonic x^2 pulse on the other hand results in a momentum space squeezing for short t . For minimal width at t_{min} , the momentum space wavefunction can be compressed down to the Heisenberg limit:

$$\sigma_x(t_f) \cdot \sigma_p(t_{min}) = x_{zpf} p_{zpf} \quad (1.13)$$

with $\sigma_x^2(t_f) = x_{zpf}^2 (1 + \omega_0^2 t_f^2)$. Thus by choosing an appropriate t_f , it is possible to create a momentum space uncertainty satisfying $\sigma_p \ll \Delta p(t)$. Since the order of the pulses doesn't matter, the harmonic and the cubic pulse can be done simultaneously.

Long Inverted Quadratic Pulse

The fringes in momentum space are mapped into position space in the far-field using another free evolution of duration t_m . This implies a linear increase in the spatial size of the fringes due to the expansion of the wavepacket. To further enlarge the fringes to a detectable size, a longer inverted harmonic $-x^2$ pulse proves useful: The position space propagator for an inverted harmonic oscillator at frequency ω_4 assuming $\omega_4 t_4 \gg 1$ reads:

$$K(x, x', t) \propto e^{\frac{i}{4x_{zpf}^2(\omega_4)}(x^2 + x'^2 - 4xx'e^{-\omega_4 t_4})} \quad (1.14)$$

Compensating the x'^2 term with an earlier short x^2 pulse, this turns into an exponentially rescaled Fourier transform. The resulting wavefunction becomes:

$$\Psi(x, t_4) = e^{\frac{ix^2}{4x_{zpf}^2(\omega_4)}} \int dx' \Psi_0(x') e^{-\frac{i}{x_{zpf}^2(\omega_4)} xx' e^{-\omega_4 t_4}} \quad (1.15)$$

Thus, with the long $-x^2$ pulse, the spatial features are exponentially magnified with $e^{\omega_4 t_4}$, dependent on the choice of intensity and duration of the pulse.

1.3 Implementation of the Pulses

The experimental realization of the previously mentioned potential landscapes (quadratic, inverted, and cubic) is implemented by a trapping scheme for nanoparticles based on a standing wave, whose phase can be changed in time. Here we discuss the corresponding implementation. Then we will show a working protocol implementing the pulses.

1.3.1 Standing Wave Potential

In general, the potential energy $V(x)$ of a particle with dipole moment $p = \alpha E(x)$ in an electromagnetic field $E(x)$ with x being the axial position around an arbitrary center x_0 can be described as [28]:

$$V(x) = -p \cdot E(x) = -\frac{\alpha}{2} E(x)^2 \quad (1.16)$$

where $\alpha = \alpha' + i\alpha''$ is the polarizability of the particle. For a standing wave with $E(x) = E_0 \cos(kx)$ at wavelength λ with wavenumber $k = 2\pi/\lambda$ and a mechanical trapping frequency [34]:

$$\omega_m = \left(\frac{6k^2 I_0}{\rho c} \text{Re} \frac{\epsilon - 1}{\epsilon + 2} \right)^{\frac{1}{2}} \quad (1.17)$$

where I_0 is the intensity of the laser beam, ρ is the mass density of the particle with mass m , c is the speed of light and ϵ is the electric permittivity, it is possible to express the standing wave potential as:

$$V(x) = -\frac{m\omega_m^2}{2k^2} \cos^2(kx) = -\frac{m\omega_m^2}{2k^2} \sum_n u_n(x_0) (x - x_0)^n \quad (1.18)$$

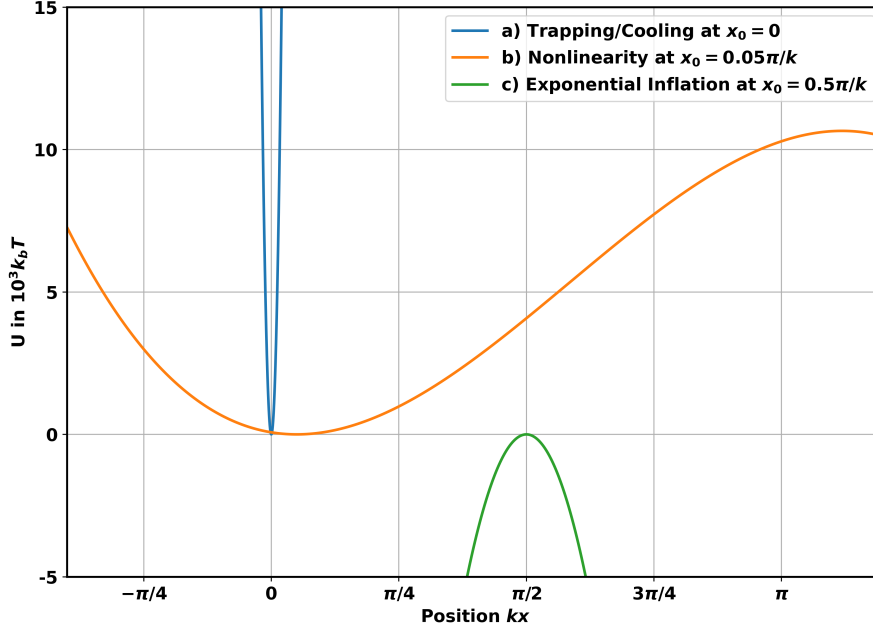


Figure 1.3: **Potential Landscapes:** They are obtained by evaluating Equation 1.19 for a) at the anti-node $kx_0 = 0$, b) between the node and anti-node at $kx_0 = 0.05\pi$, and c) the node at $kx_0 = \pi/2$ as in [18]. The evaluation is done for the parameters described in Section 2.2.1 and thus $\omega_0 = 2\pi \cdot 100$ kHz, $\omega_2 = 2\pi \cdot 2.8$ kHz, $\omega_3 = 2\pi \cdot 2.7$ kHz, $\omega_4 = 2\pi \cdot 10$ kHz, $\lambda = 1550$ nm, and $m = 7.7 \cdot 10^8$ amu.

The right part of the equation is an expansion around some point x_0 with $u_n(x) = (1/n!)(d/dx)^n \cos^2(kx)|_{x \rightarrow x_0}$. Since for a particle with a wavefunction $\Psi(x)$ of width σ_x the contribution of order n to the total potential energy $\langle \Psi | V(x) | \Psi \rangle$ is proportional to $(\sigma_x/\lambda)^n$ and usually $\sigma_x \ll \lambda$, it is assumed that all orders above $n = 3$ are strongly suppressed. Furthermore a configuration is implemented where the linear term is canceled by an appropriate electric field. Thus only terms proportional to x^2 and x^3 are considered. This leads to the following potential:

$$V(x) \approx v_2 x^2 + v_3 x^3 \quad (1.19)$$

where $v_n = -\frac{m\omega_m^2}{2k^2} u_n(x_0)$.

For trapping and cooling, the particle is positioned at the anti-node $kx_0 = 0$. As we will in Section 2.1, we will however not use a standing wave trap for the preparation of the ground-state. To create the potential landscape for the long inverted pulse, the particle has to be positioned at a node $kx_0 = \pi/2$. For the nonlinear pulse, however, the

particle has to be positioned in between a node and an anti-node, leaning towards the anti-node to ensure a positive sign for the x^2 term. The resulting potential landscapes and the required phase shift for the pulses are illustrated in Figure 1.3.

1.3.2 Full Protocol

A protocol for detectable interference fringes consists of applying the sequence of pulses described in the previous sections:

1. Start with a ground state cooled particle (Gaussian wavepacket)
2. Free evolution with duration t_f
3. Short nonlinear pulse with t_3 , $\omega_{2,3}$ and $kx_0 = 0.05\pi$
4. Free evolution with duration t_m
5. Exponential inflation with t_4 and ω_4 and $kx_0 = \pi/2$

The full protocol is shown in Figure 1.4.

In order to illustrate these steps and find the final probability distribution, one can do a full calculation starting from a ground-state cooled particle wavefunction:

$$\Psi(x, 0) = e^{-x^2/4} \quad (1.20)$$

where x is written in terms of $x_{zpf}(\omega_0)$ with ω_0 being the initial trapping and cooling frequency. All normalization constants and any consideration of decoherence effects are left out for clarity.

1. Free Evolution with Duration t_f

Starting with the first free expansion using the corresponding propagator $e^{i(x-x')^2/(4t_f\omega_0)}$ the initial wavefunction becomes:

$$\Psi(x, t_f) = e^{-bx^2 + ib_f x^2} \quad (1.21)$$

with $b = 1/(4\sigma_x^2)$, $b_f = (t_f\omega_0)/(4\sigma_x^2)$ and $\sigma_x = 1 + \omega_0^2 t_f^2$.

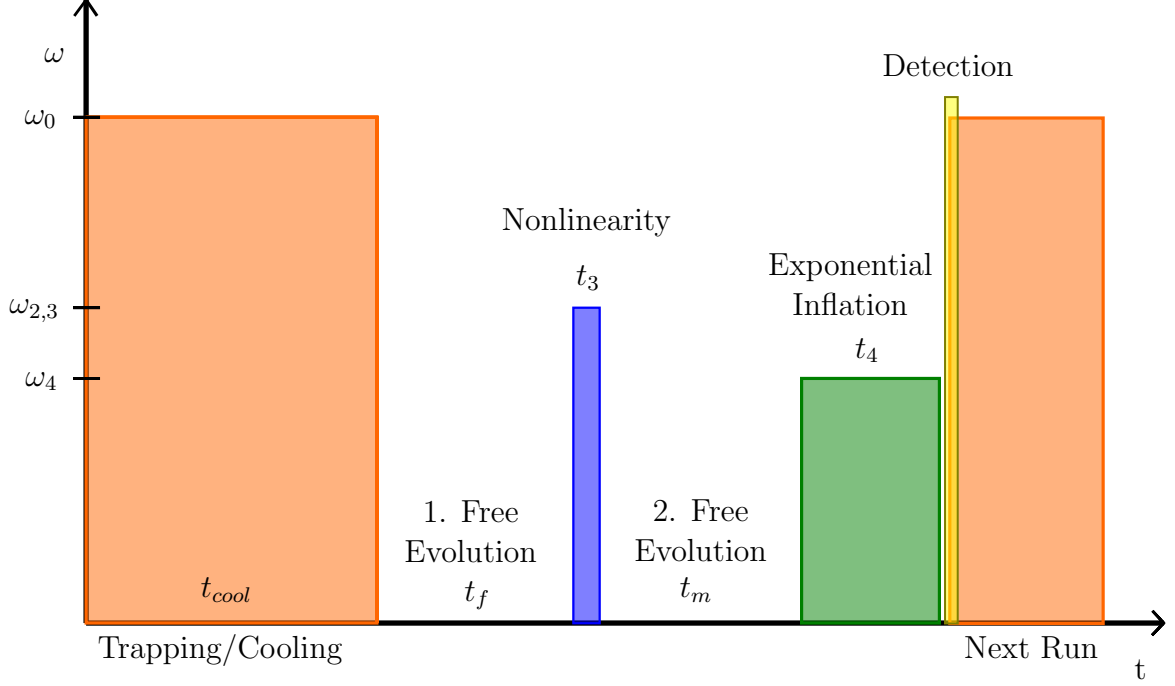


Figure 1.4: **Light Field Protocol:** Each repetition of the protocol begins with the initial ground-state cooling of the particle, at a frequency ω_0 for a duration t_{cool} . After the 1. free evolution with a duration t_f , the short nonlinear pulse follows with a frequency $\omega_{2,3}$ for a time t_3 . After another free evolution with duration t_m , the longer inverted pulse with a frequency ω_4 and duration t_4 follows. Right after the inverted pulse, the position of the particle is detected and the particle immediately cooled again to prepare for the next protocol run.

2. Short Nonlinearity with t_3 and ω_2, ω_3

After the first free expansion, the short nonlinear pulse is applied. Propagating the wavefunction of Equation 1.21 with $e^{iax^3 - (i/4)(\omega_2^2/\omega_0)t_3}$ leads to:

$$\Psi(x, t_3) = e^{iax^3 - bx^2 + ib_ix^2} \quad (1.22)$$

where

$$a = \frac{1}{6}kx_{zpf}(\omega_0) \left(\frac{\omega_3^2}{\omega_0} \right) t_3 \quad \text{and} \quad b_i = \frac{t_f\omega_0}{4\sigma_x^2} - \frac{\omega_2^2 t_3}{4\omega_0} \quad (1.23)$$

For simplicity and experimental purposes, the separate frequencies ω_2, ω_3 of this pulse will later be expressed as a combined $\omega_{2,3}$, following from Equation 1.19.

3. and 4. Free Evolution with t_m and Exponential Inflation with t_4 and ω_4

Using the propagator of a free expansion and the propagator of the long inverted pulse from Equation 1.14 leads to:

$$\Psi(x, t_4) = \int dx_1 dx_2 \Psi(x_1, t_3) e^{i \frac{(x_2 - x_1)^2}{4t_m \omega_0}} e^{\frac{i}{4} \frac{\omega_4}{\omega_0} (x^2 + x_2^2 - 4xx_2 e^{-\omega_4 t_4})} \quad (1.24)$$

For an appropriate choice of the protocol parameters, one can express the final wavefunction in the simple form:

$$\Psi(x, t_4) \propto e^{-\frac{x^2}{4\sigma_x(t_4)^2}} * \text{Airy} \left(\frac{x}{\Delta x} \right) \quad (1.25)$$

with

$$\Delta x = \sqrt[3]{3a} \left(\frac{\omega_0}{\omega_4} + t_m \omega_0 \right) e^{\omega_4 t_4} \quad (1.26)$$

Here, Δx is proportional to the fringe distance.

The position probability distribution at the end of the protocol then reads:

$$P(x) \propto \left[e^{-\frac{x^2}{4\sigma_x(t_4)^2}} * \text{Airy} \left(\frac{x}{\Delta x} \right) \right]^2 \quad (1.27)$$

Now that the fundamentals of the pulse interactions and the sequence of the protocol are explained, we will work towards experimental benchmarks for the required modulation of the light field.

Chapter 2

Light Field Protocol and Requirements

In the first chapter, we introduced the theory of a light field protocol that creates interference fringes in a ground-state cooled levitated nanoparticle. But what are parameters that produce a detectable fringe pattern and how can these parameters deviate without washing it out? Also, why do these deviations occur?

In this chapter, we provide an overview of the currently planned setup for an experimental implementation in regard to the light field. We will introduce concrete numbers and conditions for the protocol to work. We will explain possible experimental obstacles that introduce instability in the parameters of the protocol and thus lead to a change in the final probability distribution. From there we define the benchmarks necessary for the proposed control system to keep the non-Gaussian fringe pattern intact.

2.1 Experimental Implementation

This Section aims to provide an overview of the planned experimental implementation (Figure 2.1). The light field protocol itself has already been illustrated earlier and can be seen in Figure 1.4.

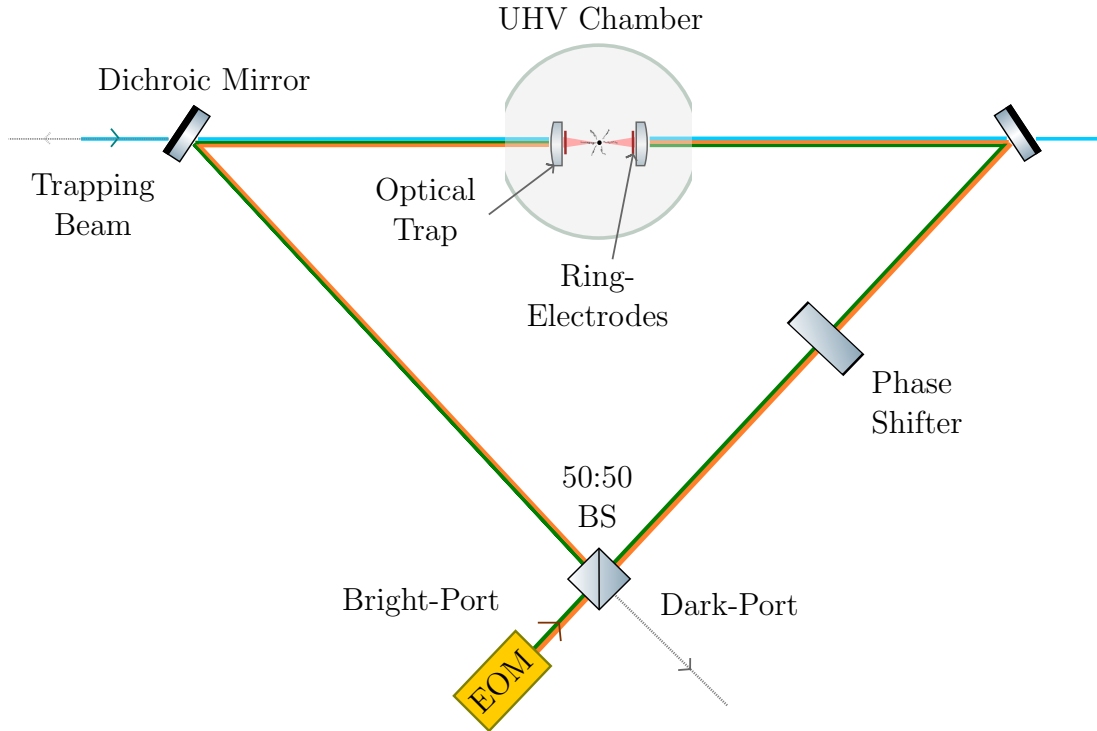


Figure 2.1: **Optical Setup for an Experimental Implementation:** The state preparation and trapping of the particle are done with a separate tweezer setup as in [21] (blue beam) that is integrated via dichroic mirrors. The non-linearity and the exponential inflation are implemented as pulses created by EOMs via a standing wave in a Sagnac interferometer (green and orange beam), where a birefringent crystal introduces a phase shift. The beam preparation is further explained in Figure 2.2 and Section 3.1. The light that is back-scattered from the particle into the interferometer mode will leave at the dark port, while the light transmitted light leaves at the bright port [29]. The optical trap is situated within a UHV chamber. Ring-electrodes control the electric field along the beam direction.

For the trapping and cooling of the particle, a single-sided tweezer configuration is introduced (blue beam) at a wavelength of $\lambda = 1064$ nm. Although this implies a single-beam gradient force trap instead of a standing wave trap, nothing changes in regards to the necessary light field modulation. We use the back-scattered light from the particle for position read-out. A complete description of the intended scheme can be found in [21, 31]. The optical trap is placed inside a UHV chamber with an expected vacuum of 10^{-10} mbar. A loading scheme using hollow-core photonic-crystal fibers is

currently under development [29, 30, 27].

The standing wave optical trap for the nonlinearity and the exponential inflation is created by two counterpropagating beams (green and orange) at a wavelength of $\lambda = 1550$ nm inside a Sagnac interferometer, integrated via dichroic mirrors, and focused in the same tweezer as used for trapping and cooling. In such an interferometer, the incoming light beam is split by a 50:50 beamsplitter into two separate arms. Two mirrors then overlap the beams at the initial beamsplitter. If well aligned, this leads to constructive interference towards the input mode of the interferometer, referred to as the bright port. If some object able to back-reflect light into the interferometer modes is situated within the Sagnac interferometer, it essentially becomes a Michelson interferometer and the back-reflected light will interfere towards the dark port. The architecture of the Sagnac inherently features high phase stability in its center position [29, 32, 33].

We use orthogonal polarizations H and V for the pulses of the nonlinearity and the exponential inflation. The required phase shift for the potential landscapes is introduced by adding a birefringent crystal, i.e. Ytterbium Vanadate, on one side of the interferometer. Such a birefringent material has different refractive indices for different transmitted polarizations, thus causing a phase difference dependent on its thickness. Together with the inherent phase stability of the Sagnac interferometer, this has the advantage of avoiding active phase shifting. We use ring-electrodes attached to the lenses to cancel the linear term of the standing wave potential (see Section 1.3.1) and for feedback cooling [29].

Initially, two separate light beams are prepared in arbitrary linear polarizations and modulated with EOMs in the form of square pulses. After leaving the optical modulators the beams are recombined at a PBS (Figure 2.2). While the vertically polarized light will be reflected, the horizontally polarized light will transmit. To ensure maximum overlap of the two beams towards the bright-port of the Sagnac interferometer, a mode-matching fiber configuration is placed at the second output mode of the PBS. By rotating the polarization in front of the PBS, the light can be adjusted for going towards either output mode. Maximizing the coupling of both beams into the mode-matching fiber results in a maximum overlap of the beams also towards the Sagnac bright-port. As follows, the initial polarization of the pulses doesn't matter for pulse modulation.

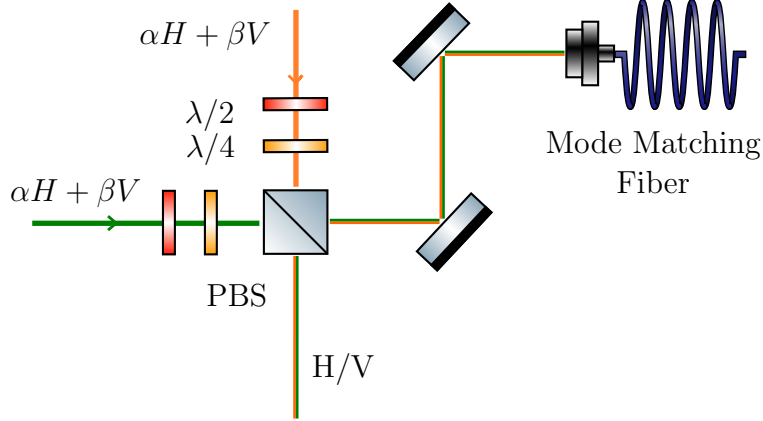


Figure 2.2: **Beam Overlap with a Mode Matching Fiber:** Both beams are separately prepared in an arbitrary polarization and modulated as required. On a PBS where H-polarized light is transmitted and V-polarized light is reflected, the beams overlap. To ensure a maximum overlap, the light is coupled into a mode-matching fiber at the opposite output mode of the PBS. The desired output mode can be adjusted by rotating $\lambda/2$ and $\lambda/4$ waveplates.

2.2 Protocol Requirements

2.2.1 Concrete Example

The parameters of the protocol have been optimized for a silica nano-sphere of $r = 50$ nm and a mass density $\rho = 2450 \text{ kg/m}^3$ [18] (Table 2.1).

ω_0	t_f	$\omega_{2,3}$	t_3	ω_4	t_4	t_m
$2\pi \cdot 100 \text{ kHz}$	1.34 ms	$2\pi \cdot 2.5 \text{ kHz}$	10 μs	$2\pi \cdot 10 \text{ kHz}$	90 μs	0.66 ms

Table 2.1: **Parameters for the Pulse Sequence:** ω_0 is the initial trapping and cooling frequency, t_f is the duration of the first free expansion, $\omega_{2,3}$ and t_3 the frequency and duration of the short nonlinear pulse, ω_4 and t_4 the frequency and duration of the long inverted quadratic pulse and t_m the duration of the second free expansion.

We assume an initial phonon occupation of $\bar{n}_x \approx 0.5$ at $\omega_0 = 2\pi \cdot 100 \text{ kHz}$ as achieved with the intended cooling setup [21]. We choose a feasible pressure of 10^{-10} mbar to ensure 90 % of experimental runs to be free of gas-particle collisions which would decohere the quantum state. Further sources of decoherence are noted in the simulation: While during the light pulses recoil scattering from the laser beam is predominant, localization from black-body radiation is relevant during the free expansions.

The predicted position distribution of the wavefunction at the end of the protocol is shown in Figure 2.3. There we identify the interference visibility as $v = (h_2 - m_1)/(h_2 +$

$m_1) = 0.23$, where h_2 and m_1 are the height of the second maxima and the first minima of the fringe pattern respectively, and a fringe spacing, defined as the distance between the first two peaks, of $\Delta x \approx 2.9$ nm.

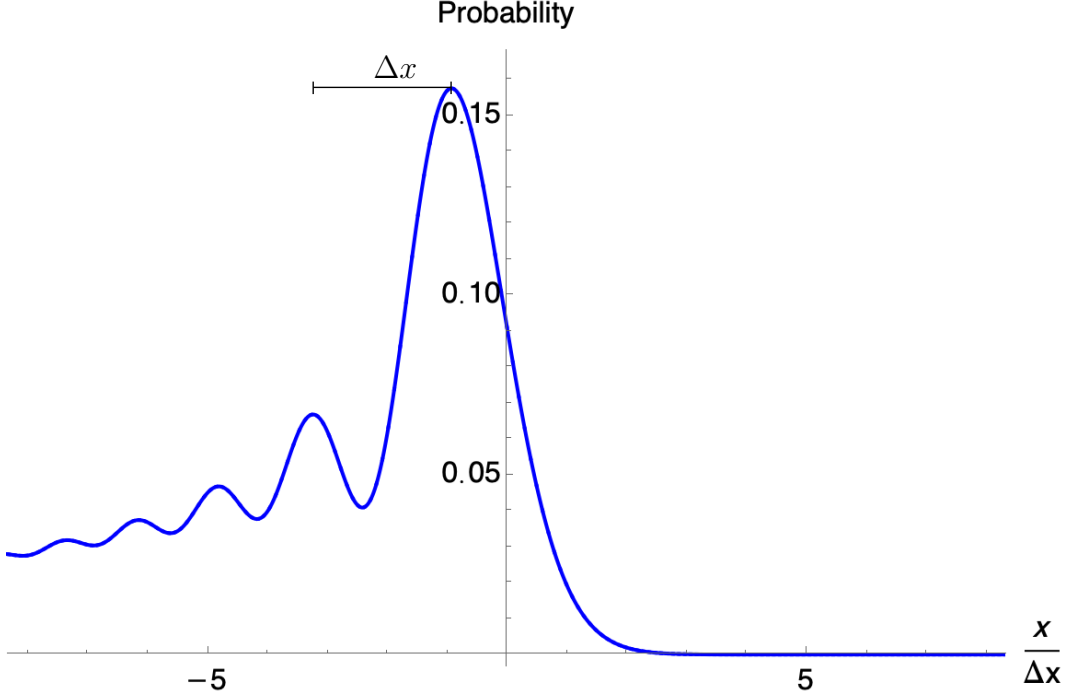


Figure 2.3: **Probability Distribution:** This plot shows the probability distribution for the parameters in Table 2.1 in terms of $x/\Delta x$, exhibiting a visibility of $v = 0.23$ and a fringe spacing of $\Delta x = 2.9$ nm.

2.2.2 Precision Requirements on the Experimental Parameters

The EOMs creating the optical pulses, in our case square pulses, are controlled by an electronic drive signal. The targeted pulses are, however, imperfect. Figure 2.4 shows a comparison of an ideal square pulse with a realistic pulse in terms of optical power over time. While the ideal pulse represents an ideal square instantly going from absolute zero power to the desired maximum power and back, the real pulse shows deviations.

We see, that the minimum power is not zero, but a finite value P_{low} . By comparing this to the maximum power P_{high} , we specify the extinction ratio of the signal $R_{ext} = P_{low}/P_{high}$. The maximum power is also noisy. This can be caused by the background noise of the electronic drive, e.g. Johnson-Nyquist noise from the circuit or ground noise, and intensity noise of the laser source and leads to an uncertainty of the power

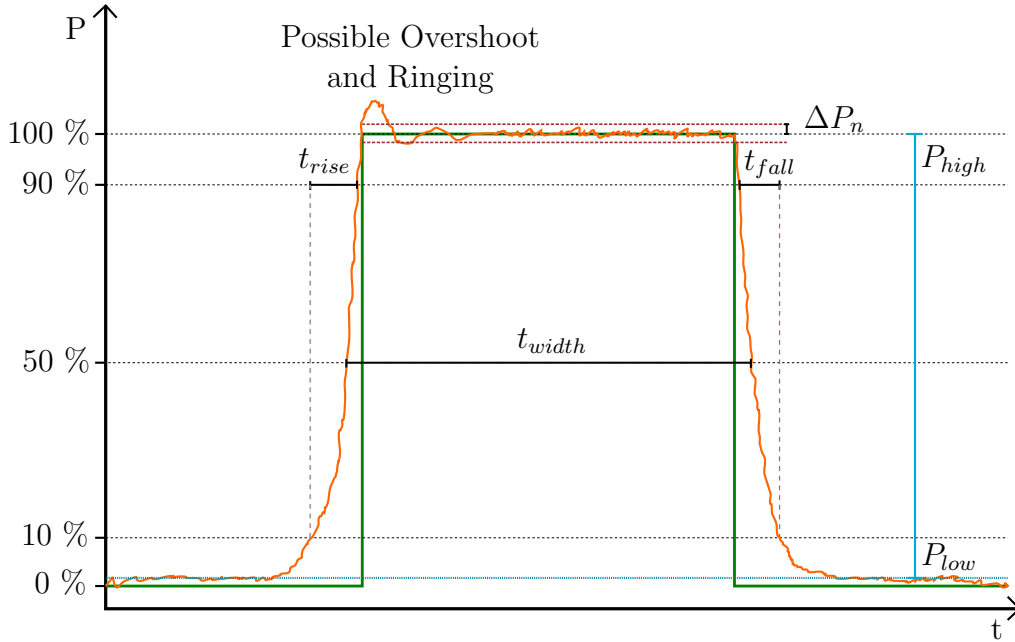


Figure 2.4: **Pulse Properties:** Comparing a realistic optical pulse (orange) to an ideal pulse (green) shows several deviations. The realistic optical pulse does not reach the zero power level, but some light P_{low} remains. Comparing this to the high power level P_{high} yields the extinction ratio of the signal. Furthermore, it shows a constant jitter in its intensity, causing a certain width in power ΔP_n . Slower fluctuations in power also lead to a change in the mean peak level of the pulse ΔP over many repetitions. The edges of the pulse have a limited rise and fall time between the 10 % and 90 % power level denoted by t_{rise} and t_{fall} . The width of the pulse t_{width} , defined as the time from 50 % to 50 % of the peak level, can also deviate in time with Δt_{width} . The same is true for a space between pulses t_{space} .

maximum ΔP_n , where n denotes a single pulse. Furthermore, if the electronic drive, as well as the laser source, also have power fluctuations at lower frequencies compared to the pulse frequency, the mean of the maximum power level of a sequence of pulses will also fluctuate over time with ΔP . An overshoot in the rise or an undershoot in the fall, caused by an impedance mismatch, followed by ringing until a constant power level settles, is also typical for electronic pulse signals. Often this is designed on purpose to achieve a faster rise- and fall time.

Regarding the time scale, the realistic pulse shows finite rise and fall times t_{rise} and t_{fall} , characterized as the required time to rise or fall between 10 % and 90% of the pulse peak level. This is limited by the response time of the optical modulator due to its capacitance and by the circuit of the driving signal due to stray capacitance and inductance [39]. The width of the pulse t_{width} , measured as the duration from 50 % to 50 % of the peak level, can also vary in time as Δt_{width} . This is caused by phase noise

and jitter of the clock of the electronic circuit and is likewise true for the deviation of the space between two pulses Δt_{space} .

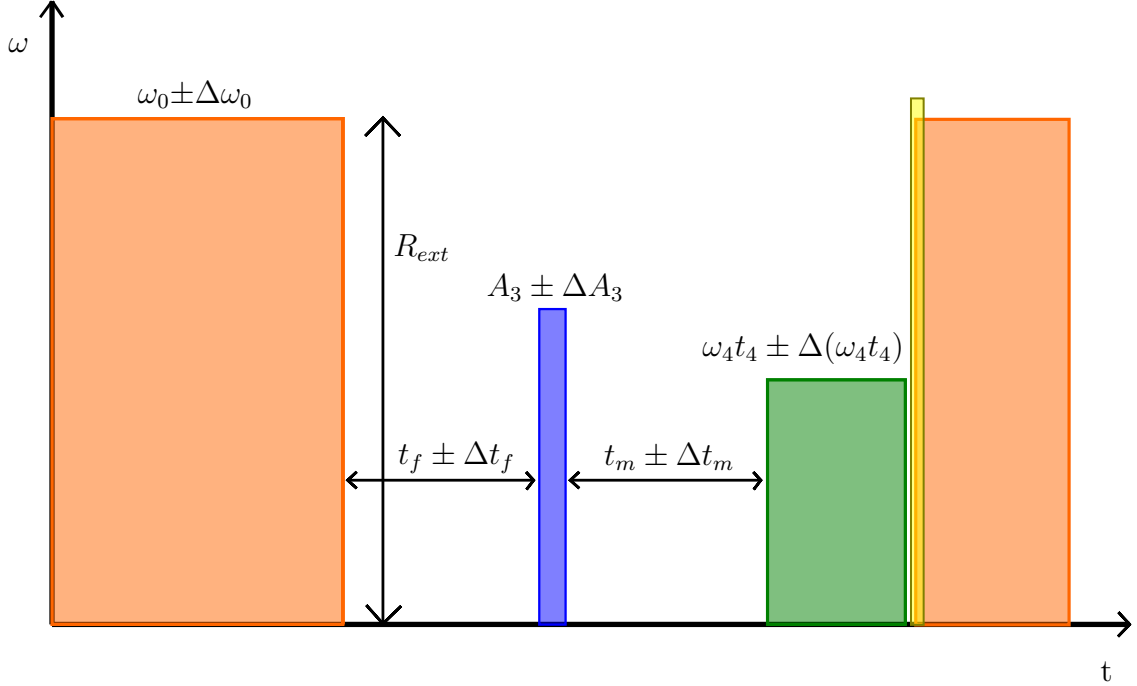


Figure 2.5: **Light Field Benchmarks:** The fluctuations of the pulse power contribute to errors $\omega_0 \pm \Delta\omega_0$ and $\omega_4 t_4 \pm \Delta(\omega_4 t_4)$. Δt_{width} also contributes to $\Delta(\omega_4 t_4)$. The fluctuations in Δt_{space} lead to errors on $t_f \pm \Delta t_f$ and $t_m \pm \Delta t_m$. Regarding the nonlinear pulse, only the pulse area matters with $A_3 \pm \Delta A_3$. The minimum achievable power P_{low} and the maximum power P_{high} yield the extinction ratio R_{ext} .

These imperfections have consequences for the desired protocol. The fluctuations in power ΔP and ΔP_n lead to a deviation of ω_0 , $\omega_{2,3}$, and ω_4 . For the trapping we thus have an uncertainty $\omega_0 \pm \Delta\omega_0$. Similarly, the Δt_{width} and Δt_{space} of the pulses lead to deviations of the time durations in the protocol t_f , t_m , t_3 , and t_4 . The additional jitter and noise as well as possible over- and undershoots or ringing further contribute to deviations in the energy of the pulse, given by the integrated power and thus the area of the pulse. This is relevant for the short nonlinearity with $A_3 \pm \Delta A_3$. As the final probability distribution in Equation 1.27 shows, the effect of the exponential inflation is dependent on the product of $\omega_4 t_4$ and thus we find $\omega_4 t_4 \pm \Delta(\omega_4 t_4)$ to be relevant. All affected parameters are illustrated in Figure 2.5.

The protocol has to be repeated many times to acquire statistics to reconstruct the probability distribution. As a change in the parameters of the protocol leads to a change in the probability distribution, it needs to be ensured that a certain precision is kept along a sufficient number of repetitions to guarantee an overlap of the fringes. If

the pattern is varying too much, the fringes would become indistinct and the visibility drops. We will now investigate the necessary benchmarks for successful detection.

Extinction Ratio

While in theory, a free expansion assumes no interaction of the particle with any light leading to a free evolution of the wavepacket, this is not necessarily the case in an experimental environment. Usually, optical modulators have some leftover light in their minimum possible throughput. This can e.g. be caused by stray light from scattering effects.

Assuming that there is still some light in the standing wave during a free expansion for an initial frequency ω_i , it is possible to investigate whether this has a notable effect. The remaining light represents a weak oscillator with some frequency $\omega_{ff} = \omega_i \sqrt{R_{ext}}$ that acts for the time of the free expansion. If during this time $\omega_{ff} t_{f,m} \ll 1$, the effect is negligible as the propagator for the harmonic oscillator can then be approximated with the free particle propagator. We choose $\omega_{ff} t_{f,m} < 0.05$ taking into account an approximation error of 5 %. This fulfilled for $\omega_0 = 2\pi \cdot 100$ kHz at an extinction ratio of $R_{ext} \leq 3 \cdot 10^{-9}$.

Pulse Area of the Short Pulse

The short nonlinearity is the most sensitive part of the protocol. This is because a change in the momentum kick p_0 of the pulse will result in a change in the fringe spacing. As a measure of the energy of the pulse, only the pulse area A_3 matters. The pulse area is not only influenced by ΔP and Δt_{width} , but all possible noise effects as shown in Figure 2.4. To ensure that the fringes don't get washed out, the standard deviation of the momentum kick σ_{p_0} , which is proportional to the pulse area, should be at least 5 times smaller than the fringe spacing:

$$p = \frac{\sigma_{p_0}}{p_0} < \frac{(3a)^{1/3}}{5p_0} \approx 0.7 \cdot 10^{-5} \quad (2.1)$$

where

$$p_0 = \frac{1}{k^2 x_{zp}(\omega_0)} \frac{\omega_m^2 t_3}{\omega_0} u_1(x_0) \quad (2.2)$$

Thus we set our benchmark for the relative uncertainty on the area at $\Delta A_3/A_3 \leq 0.7 \cdot 10^{-5}$. Assuming the above precondition together with a negligible R_{ext} fulfilled and thus the initial fringe spacing deviating by less than 20 %, we choose the allowed deviations for the remaining parameters $\Delta\omega_0$, Δt_f , Δt_m , and $\Delta(\omega_4 t_4)$ such that it doesn't cause a further significant impact on the final probability distribution. For finding the required precisions, we present a simulation provided by Lukas Neumeier that allows us to plot and characterize the overlap of a deviated with the initial probability distribution by calculating the fidelity. The simulation assumes absolute zero power during free expansions as well as a constant $\Delta A_3 = 0$. It includes all considerations in [18].

The overlap of two quantum states can be quantified using the fidelity F , where in general for $F = 1$ the states are identical, and for $F = 0$ the states are certainly distinct. For two states ρ and σ the fidelity reads [43]:

$$F(\rho, \sigma) = \left(\text{tr} \sqrt{\sqrt{\rho} \sigma \sqrt{\rho}} \right)^2 \quad (2.3)$$

If we now compare two normalized probability distributions $P_1(x)$ and $P_2(x)$, where one has a deviated parameter set in regards of $\Delta\omega_0$, Δt_f , Δt_m , and $\Delta(\omega_4 t_4)$, we can calculate the fidelity of the two in some finite region $x_1 \rightarrow x_2$ as:

$$F(P_1, P_2) = \left(\int_{x_1}^{x_2} \sqrt{P_1(x) P_2(x)} \right)^2 \quad (2.4)$$

We limit the region to ± 15 in units of $x/\Delta x$, since this contains the main visible features.

Initial Trapping and Cooling

A change in ω_0 mainly affects the amplitude of the fringe maxima. While an increase in ω_0 shifts the amplitude distribution towards the left and thus in general lowers the first two peaks, a decrease in ω_0 shifts the amplitude towards the first peaks at the right but at the same time lowers the visibility of the fringes. This is because for low ω_0 the momentum space squeezing is reduced. Choosing a relative error of $\Delta\omega_0/\omega_0 \leq 5 \cdot 10^{-2}$ leads to only a barely visible change in the distribution by slightly shifting the first peak up or down and keeps a fidelity of $F = 0.99998$, both for an increase or decrease of ω_0 .

Timing Precision on t_f and t_m

A shift in time duration Δt_f of the first free expansion has a similar effect on the final density function as a change of ω_0 as can be reasoned by Equation 1.21. While an increase of t_f lowers the first peaks, a decrease leads to higher peaks but lowers the visibility. A change in the duration of the second free expansion shows slightly different behavior. A change of t_m shows similarities to a change in t_f , but additionally, an increase of t_m shifts the fringes away from the first maximum while a decrease of t_m compresses them towards the first maxima. In comparison to the first free expansion, the second free expansion already acts on the fringe pattern resulting from the non-linear interaction. A change in duration changes the expansion of the features. Choosing a $\Delta t_m = \Delta t_f = 1$ ns keeps the fidelity above $F = 0.99999$, both for an increase or decrease of t_f and t_m .

The timing precision only matters during a single protocol run. This means that only the timing of events related to the start of one protocol, at the moment the cooling is turned off and the first free expansion starts, is investigated. Whether the total duration of thousands of repetitions is repeatable doesn't change the measurement outcome. At the end of every single run, the position of the particle is measured and the information stored. After that, the protocol starts again once the cooling is turned off.

Precision on the Exponential Inflation

Equations 1.15 and 1.26 show that the exponential inflation of the long inverted $-x^2$ pulse is scaling with $\omega_4 t_4$. An increase or decrease of this product generally leads to a weaker or stronger exponential magnification of the fringe pattern. Choosing a relative error $\Delta(\omega_4 t_4)/(\omega_4 t_4) \leq 3 \cdot 10^{-3}$ keeps the fidelity above $F = 0.9995$. This implies both a possible increase or decrease of $\omega_4 t_4$.

Interplay of $\Delta\omega_0$, Δt_f , Δt_m and $\Delta(\omega_4 t_4)$

What happens now if $\Delta\omega_0$, Δt_f , Δt_m , and $\Delta(\omega_4 t_4)$ are deviating simultaneously? Staying within the previously set benchmarks, the fidelity stays above $F = 0.9995$ for an increase or decrease of the parameters respectively. A plot of a simulation comparing corresponding deviated probability distributions with the initial one is shown in Figure

2.6. We find the fringe spacing to deviate with ± 0.08 nm.

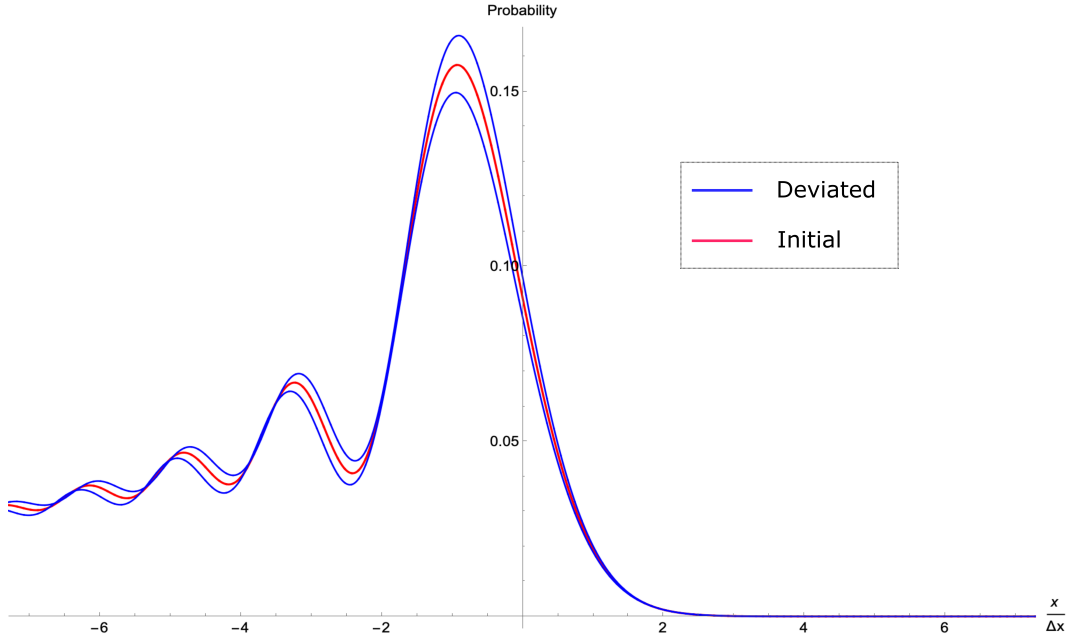


Figure 2.6: **Simulated Deviated Probability Distributions:** The two **blue** lines show the deviated probability distributions in regards of the defined benchmarks, both for an increase and decrease of the parameters. This represents both extreme cases of drifts of the fringes within: A relative error $\Delta\omega_0/\omega_0 \leq 1 \cdot 10^{-2}$, $\Delta t_f = \pm 1$ ns, $\Delta t_m = \pm 1$ ns, and a relative error $\Delta(\omega_4 t_4)/(\omega_4 t_4) \leq 1 \cdot 10^{-3}$, while R_{ext} is neglected and $\Delta A_3 = 0$. The **red** line shows the initial distribution as in Figure 2.3. This leads to a deviation of $\approx \pm 0.08$ nm for the fringe spacing.

Summary of the Chapter

In conclusion, we presented an overview of the experimental implementation of the protocol. The control of the light field is a core element of the scheme. It can be analyzed independently. We introduced concrete parameters for the light control and investigated possible experimental deviations and fluctuations caused by the pulse modulation with an EOM and the required electronic drive. By studying the effects of these deviations, we defined benchmarks for the deviations of the parameters that ensure the detection of interference. We find that the necessary precision on the experimental parameters are: $R_{ext} = 3 \cdot 10^{-9}$, $\Delta A_3/A_3 \leq 0.7 \cdot 10^{-5}$, $\Delta\omega_0/\omega_0 \leq 1 \cdot 10^{-2}$, $\Delta t = 1$ ns, and $\Delta(\omega_4 t_4)/(\omega_4 t_4) \leq 1 \cdot 10^{-3}$.

In the next chapter, we will present and characterize a control system and test the performance against these benchmarks.

Chapter 3

Programmable High-Precision Control of the Light Field

In the previous chapter, a brief overview of our planned experiment on nonlinear quantum dynamics was given. From this, we identified a set of parameters specifically concerning the control of the light fields that are crucial to the successful implementation. We discussed benchmarks for allowed deviations from these parameters that will leave the final signature of a successful experiment, i.e. the interference fringes, intact. In this chapter, we show that a configuration of an AOM, EOM, and a state-of-the-art electronic control board (Sinara) allows for reaching most of the necessary specifications. We will present measurements testing the relevant parameters discussed in section 2.2.2: R_{ext} , $\Delta\omega_0/\omega_0$, $\Delta t_{f,m}$, $\Delta A_3/A_3$, and $\Delta(\omega_4 t_4)/(\omega_4 t_4)$. We will conclude by discussing strategies to improve on these results to meet our benchmarks.

3.1 Electro-Optic Implementation: Test Setup

Electro-Optic Modulators

The working principle of electro-optic modulators, in our case Mach-Zehnder type intensity modulators, is based on the electro-optic effect. By applying a voltage or voltage modulation to a port of the EOM, the refractive index of the internal LiNbO₃-crystal is changed, and thus the speed of light traveling through it. This leads to a difference in phase in the internal interferometer paths which in turn changes the output intensity. This can be described mathematically as [35]:

$$I_{out}(t) = T_{mod} \frac{I_{in}}{2} \left[1 + \cos \left(\frac{\pi}{V_{\pi}} V(t) - \Phi \right) \right] \quad (3.1)$$

where I_{in}, I_{out} is the in-/output intensity, T_{mod} is the optical transmission of the device, V_{π} is the half-wave π -voltage and Φ a phase term.

EOMs usually feature two different ports. One is a coaxial RF-port that is used for applying the desired modulation signal. The second is a bias port that is used for compensating possible drifts of the EOM due to environmental changes, e.g. temperature or humidity. This can be accomplished by manually adjusting the applied voltage such that the optical output power is locked to a chosen setpoint or by implementing an automatic feedback system. The setpoint can for example be minimum or maximum output power as the reference from which the signal is modulated at the RF-port.

Two different EOMs are used for later measurements. EOM 1 is an iXblue MXAN-LN-20-00-P-P-FA-FA-HOP, a custom production 1550 nm 20 GHz intensity modulator that allows high optical input powers up to 500 mW. Since it has an insertion loss of about 3.5 dB according to its datasheet, the maximum guaranteed output is reduced to 220 mW. The second EOM is a standard iXblue 1550 nm 10 GHz MX-LN-10, limited to a guaranteed output of 45 mW. EOM 2 will only be used to measure the timing precision of two separate EOMs.

Optical Setup

For measuring the required parameters, an optical setup with light modulators is used. The basic configuration is displayed in Figure 3.1.

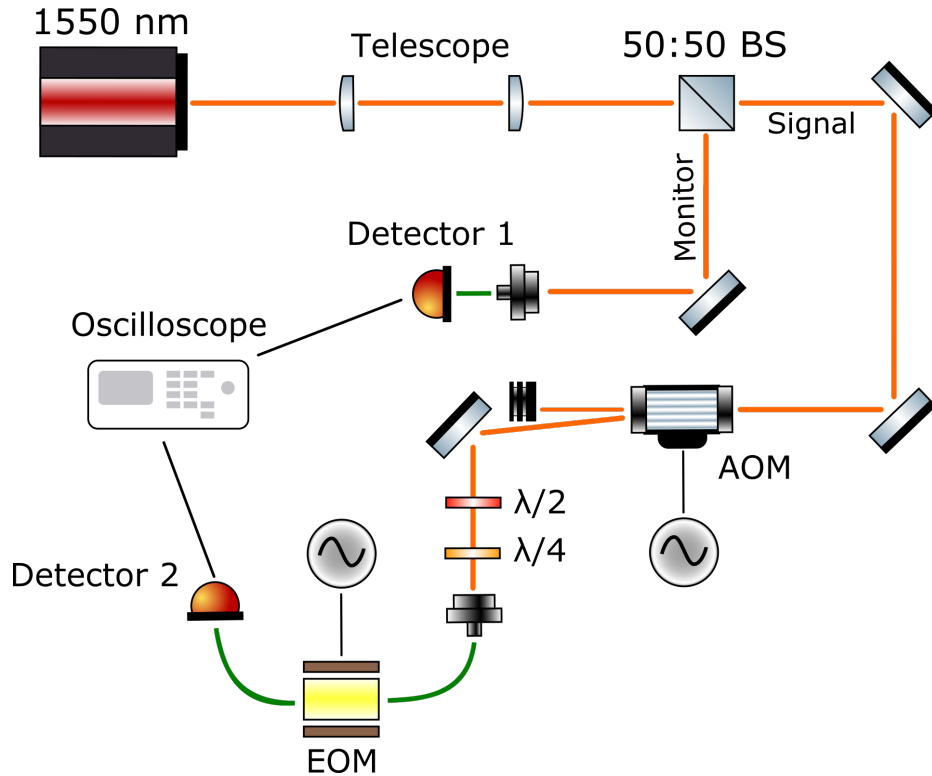


Figure 3.1: **Optical Setup for Characterizing the Light Field Control:** The setup uses a 1550 nm laser as a source that is power-monitored using a 50:50 BS. The signal path first passes a free-space AOM before it is coupled into the optical fiber of an EOM. The signal of both detectors is recorded with an oscilloscope.

The laser source of the setup is a 1550 nm "Koheras Adjustik E15" seeder by NKT photonics, amplified by a "Koheras Boostik HPA" fiber amplifier of the same manufacturer. This is the same laser planned to be used for the full experiment. The waist at the laser's output is 2 mm. We build a 4:1 telescope to decrease it to 0.5 mm, the recommended diameter for the AOM. Right after the telescope, a 50:50 beamsplitter splits the light into two different arms. The reflected arm will be used for monitoring the optical input power. A mirror and a fixed-focus collimation package couple the light into a single-mode fiber going to a photodetector (Thorlabs DET08CFC/M). The output of the detector is linked to a Picoscope 5444D serving as the oscilloscope for read-out. For some measurements, a faster Teledyne LeCroy Wavepro 760-ZI is used instead where mentioned explicitly. An appropriate 50 Ohm BNC feedthrough terminator (Thorlabs T4119) ensures the maximum signal bandwidth of 5 GHz of the detector.

The signal arm is transmitted at the beamsplitter and passes through an AOM which is one type of optical modulators that will be used. The power in the first-order mode

is proportional to the RF driving power but will saturate towards its maximum of 36 dBm. Note that at no applied drive, the signal does not vanish due to scattering. The AOM in the setup is a custom 1550 nm Gooch & Housego AOM (3080-197) with a center frequency of 80 MHz.

After the AOM, the beam is coupled into a fiber-based EOM. Since it has PM fibers, waveplates are used to adjust the polarization. The output fiber of the EOM is connected to a second Thorlabs DET08CFC/M detector that goes to the oscilloscope.

3.2 Electronic Circuit

The optical modulators in the setup are controlled by electronic signals. The signal chain from the source to the devices follows three main steps. The main source and control basis is the Sinara/ARTIQ ecosystem, claiming nanosecond timing resolution and high synchronicity among its outputs. ARTIQ is the software environment where the desired signals and their logic are programmed and Sinara is the hardware outputting them. After the Sinara, the created signals follow an electronic circuit necessary to appropriately drive the modulators.

3.2.1 Signal Processing in Sinara

Sinara is an open modular hardware project integrated into the ARTIQ ecosystem (see Section 3.2.3). All related information including schematics and detailed technical specifications can be found in detail on the Sinara Github page [36]. The Sinara used for the measurements in this thesis consists of several different modules. A photo of the front panel of the device is shown in Figure 3.2.

The base module acting as the ARTIQ master is called Kasli. Kasli is an FPGA carrier capable of controlling up to 12 different Eurocard-extension-modules (EEM). It is connected to a computer via a Netgear GS110TUP gigabit ethernet switch using the SPF-0 port on the front panel. The remaining SPF ports can be used for connections in a master/slave configuration, allowing the system to be expanded above the limits of one Kasli.

For coordination of actions in the device, the Clocker module distributes a low jitter clock signal up to 1 GHz among the cards. It features an input for using an external



Figure 3.2: **Frontpanel of the Sinara and its Modules:** From left to right: Kasli FPGA-carrier, 3x DIO-SMA, Clocker, 2x Urukul, Sampler ADC, Fastino DAC, and its corresponding IDC-SMA and IDC-BNC adapter.

reference clock and 10 outputs including 4 externally accessible SMA outputs that can be used for synchronizing additional external devices to the Sinara.

Urukul is a 4-channel 1 GS/s DDS-based frequency synthesizer in the EEM form factor. Our version is based on the AD9912, featuring a 47-bit down to $8\mu\text{Hz}$ frequency and 14-bit phase-offset resolution at an output of 1-400 Mhz. A digital step-attenuator with a range of 0 to -31.5 dB and 0.5 dB steps can be used for adjusting the output amplitude. In our case, the Urukul is used for driving and controlling the AOMs.

The digital input-output DIO-SMA cards with selectable direction and termination can supply valid TTL levels into 50 Ohm with a minimum pulse width of 5 ns. Thus it can be used with any TTL- or CMOS-logic compatible devices. Each card has overall 2 banks with 4 channels each. In our case, it is used for the control of all devices compatible with TTL logic. The DIO-SMA will control the logic of the EOM pulses.

Moreover, the Fastino is a fast 32-channel, 3 MS/s per channel, 16-bit DAC EEM card with a $\pm 10\text{ V}$ output range. By using additional IDC-SMA and IDC-BNC adapter cards, the outputs can be accessed via SMA and BNC ports. Due to its quick update rate of $1\ \mu\text{s}$, it can for example be used in servo applications in combination with an ADC such as the Sampler.

The Sampler module is an 8-channel 16-bit ADC EEM with an update rate of up to 1.5 MS/s.

3.2.2 Signal Chain

Driving our AOM requires up to 36 dBm power while the Urukul only provides a maximum of 10 dBm. We thus amplify the Urukul signal for AOM driving by an additional Mini-Circuits ZHL-2W-1+ amplifier. The modulation of the AOM output in the first-order diffraction is accomplished by modulating the amplitude of the driving signal. This can be done either by changing the output attenuation of the Urukul or by just simply turning the output on and off for modulating down to the minimum. Both are limited to a glitch time of 100 ns by internal components of Urukul such as the RF switch HMC349ALP4CE with a rise and fall time of 60 ns. Using an external Mini-Circuits ZASWA-2-50DR+ switch that has an on-/off switching performance of 20 ns did not improve the rise-/fall time of the AOM any further and was thus left out for simplicity of the circuit and for avoiding potential additional noise. The full signal chain is shown in Figure 3.3.

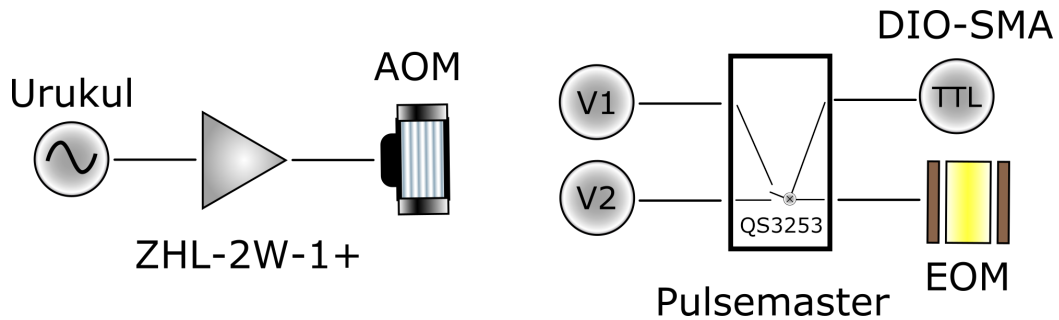


Figure 3.3: **Signal Chain from Sinara to the AOM and EOM:** Left: The Urukul output is amplified by a Mini-Circuits ZHL-2W-1+ before it reaches the AOM. Right: The Pulsemaster receives two different voltage levels. A zero-voltage V1 and a higher voltage V2. Controlled by TTL-logic of the Sinara DIO-SMA, a QS3253 multiplexer switches between these voltages creating a pulse signal for the EOM.

The EOMs on the other hand require direct electronic pulse signals to create pulses in the light field. To retain compatibility with Sinara and ARTIQ and for easy accessibility of the degrees of freedom, a highspeed CMOS/TTL quick-switch QS3253 multiplexer by Renesas is used for this purpose. While the Sinara TTL output from the DIO-SMA module serves as the switching control logic, the applied voltages at the inputs can

easily be adjusted, even in ARTIQ when using the output of the Fastino DAC. While the QS3253 is a 4:1 multiplexer, a QS3251 would even feature 8:1, making it possible to switch between 8 different inputs ranging from -0.5 V to 7 V, enough to cover the full modulation depth of the EOM. For the measurements in this thesis, only two inputs are necessary since only on-/off pulses are recorded. For this purpose, the QS3253 is mounted in a case with SMA and BNC connectors as shown in Figure 3.4, called the Pulsemaster.



Figure 3.4: **The Pulsemaster:** It features two separate QS3253 multiplexers of which only two inputs are used in each, making it a two-channel TTL-controlled pulse-generator. While on one side there are BNC connectors for applying the DC-levels one intends to switch, the other side has SMA connectors that feature an output port and a logic control input for each channel (see Figure 3.3).

For the bias control of the EOM, an automated system MBC-DG-LAB by iXblue was not able to find a more stable setpoint for the optical output power compared to a manual adjustment for the timescales of the measurements. Thus the bias voltage was manually adjusted for the measurements by setting an appropriate DC level at the EOM bias port with a Tektronix AFG3152C waveform generator. The chosen bias setpoint for our pulse application is minimum optical output. This enables modulation starting from the optical power minimum, beneficial for a high extinction ratio.

3.2.3 Logic Protocol and Coding in ARTIQ

ARTIQ (Advanced Real-Time Infrastructure for Quantum physics) is an open-source control system designed for quantum information experiments maintained and developed by M-Labs. It is well suited for our purpose since we need high timing precision with the ability to keep this precision synchronously along with multiple different signals. ARTIQ features a high-level programming language based on Python, reaching nanosecond timing resolution and sub-microsecond latency on dedicated FPGA hardware such as the Kasli in the Sinara [37].

The experimental protocol is executed in form of a python program as an ARTIQ "kernel" on the core device Kasli. After initializing the desired channels of the Sinara modules and setting parameters, any protocol using the functions of the modules can be built with a timing resolution in units as small as 1 ns.

To illustrate the programming of the protocols used in this thesis, a few short examples are given. The first example for a short 10 μ s TTL pulse of channel 0 of the DIO-SMA is:

```
tt10.output()    #Set DIO Channel 0 as output
tt10.on()        #Set DIO Channel 0 to high
delay(10*us)     #Delay of 10 us
tt10.off()       #Set DIO Channel 0 to low
```

In combination with the Pulsemaster, this causes a switch from low to high voltage and back to low after 10 μ s. It can also be simplified to a single command if an advance of the time cursor is appropriate during the pulse:

```
tt10.output()    #Set DIO Channel 0 as output
tt10.pulse(10*us) #Chanel 0 10 us pulse
```

Similarly, it is possible to control the output of the Urukul module used for driving the AOM. A 10 μ s pulse after setting the initial frequency, phase and attenuation could look like this:

```
self.urukul0_ch0.init()           #Initialize Channel 0
freq = 80*MHz                     #Set parameters
attenuation = 2.0
self.urukul0_ch0.set_att(attenuation)
self.urukul0_ch0.set(freq, phase = 0.0)
```

```

self.urukul0_ch0.sw.on()           #Channel on
delay(10*us)                       #Delay of 10 us
self.urukul0_ch0.sw.off()        #Channel off

```

The advance of the time cursor does not allow simultaneous actions. It will wait until the specified pulse is done.

Since ARTIQ is based on Python, it is possible to now use features like loops for multiple repetitions. If for example it is required to have 1000 $10\ \mu\text{s}$ TTL pulses with 1 ms space in between, one can write:

```

tt10.output()
for i in range(1000):             #Repeat for 1000 times
    tt10.pulse(10*us)            #Channel 0 10 us pulse
    delay(1*ms)                  #Delay for 1 ms

```

In this way, it is possible to configure any desired pulse protocol. Further reference on ARTIQ, its specifications, working principle, and language can be found in the ARTIQ manual [38].

3.3 Measurements

3.3.1 Preliminary Measurements

Detector Calibration and Pulse Behavior

In advance of performing any measurements, a power calibration is done for the given DET08CFC/M Thorlabs detector in combination with a Picoscope 5444D serving as the oscilloscope. This is important for a conversion of the measured detector output voltage into optical power as the desired unit to be displayed. The calibration factor is attained by measuring several different optical input powers and comparing them to the measured detector output voltage. The obtained linear regression of the acquired data (Figure 3.5) yields the calibration factor in its slope, together with an offset.

Secondly, very small optical powers down to the order of $30\ \mu\text{W}$ are required for the short pulses, but the detector together with the minimum range of the oscilloscope ($\pm 10\ \text{mV}$) requires higher optical powers to show a significant signal. A measurement is done to investigate whether different pulse power levels scale linearly. For this purpose, the

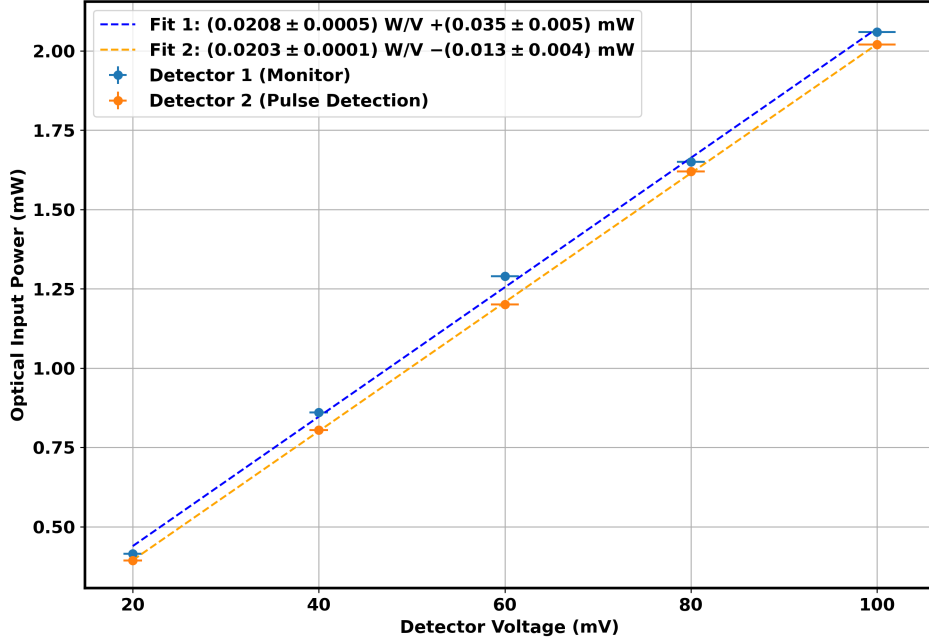


Figure 3.5: **Calibration of the Detector Output Voltage to the Optical Input Power:** A linear regression yields the corresponding calibration factor and offset. From this, the recorded detector voltage (mV) can be converted into optical power (mW).

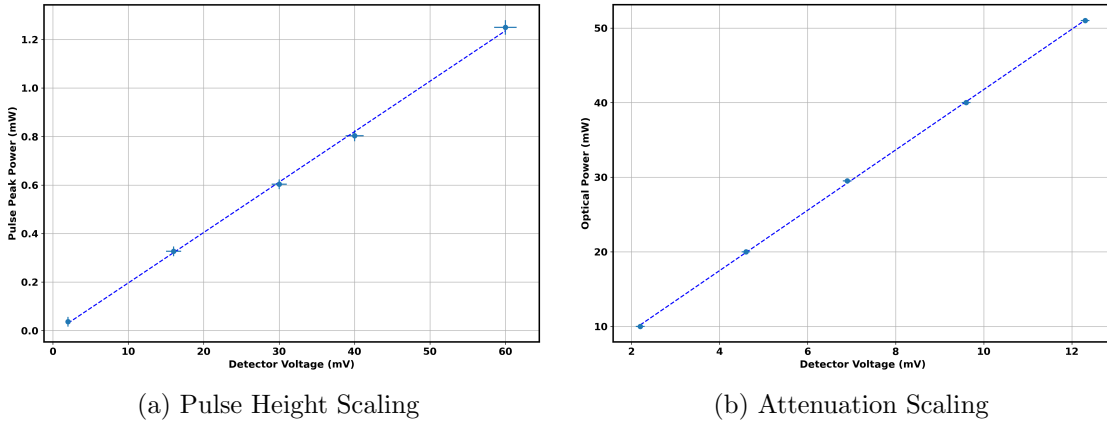


Figure 3.6: **Power Scaling:** a) Recording pulses at different powers shows a linear behavior with a mean squared error of $0.00013 (mW)^2$. b) Adding density filters for attenuation in the free-space part before the coupler also suggests linear behavior with a mean squared error of $0.03 (mW)^2$. Thus it is assumed that it is valid to record pulses at higher powers and make conclusions on lower powers. This will be relevant when recording at optical powers that would, without attenuation, saturate the detector, as for ω_0 , or when investigating pulses that would, due to their required low powers, only be barely visible with the given detector and oscilloscope.

same pulse is recorded at different optical input powers and the scaling is investigated. This is only done for detector 2 which is used for later measurements of these pulses, while detector 1 will only be needed for measuring the timing precision of pulses from

separate optical modulators and for power monitoring. The obtained graph is displayed in Figure 3.6.

Similarly, a measurement is done at even higher optical input powers, measured with a power meter, with a series of density filters (Thorlabs ND03A, NENIR02A, ND04A, NE05A) before the detector. The filters are placed in front of the coupler and in sum have an optical density of 1.4 and thus a transmission of 4 %. This is to investigate changes in the linearity of the power. This is done with detector 2 only as well. The measurements suggest that the power shows a linear behavior in both cases. Thus we estimate the real power given a measurement of higher power. Furthermore, we assume that the timing of pulses is independent of power.

V_π and Extinction Ratio of the EOM's

When working with EOMs, it is useful to characterize the V_π (Equation 3.1). It is the maximum required voltage for any accessible output power. In such a measurement it is possible to read out the maximum possible extinction ratio of the EOM as well.

A 50 kHz, $\pm 5V$ triangular wave is applied to the RF port of the EOM. This causes a sinusoidal output of the EOM as shown by Equation 3.1. From fitting the resulting optical power it is now possible to acquire the applied voltage difference necessary to go from minimum to maximum intensity (Figure 3.7), that is V_π . For each EOM, 200 single measurements were taken over a period of 10 seconds and the mean and its deviation were calculated for both the π -voltage and the extinction ratio. The results are shown in Table 3.1.

For the measured extinction ratio of $(1.3 \pm 0.3) \cdot 10^{-3}$ of EOM 1, an initial trapping and cooling frequency of $\omega_0 = 2\pi \cdot 100$ kHz with a relative deviation of $\Delta\omega_0 = 5 \cdot 10^{-2}$ at a free expansion time of $t_m = 1.34$ ms still corresponds to 30 ± 7 oscillations and thus doesn't satisfy the criteria of $\omega_{ff}t_{f,m} < 0.05$ introduced in Section 2.2.2.

	EOM 1	EOM 2
π -Voltage (V)	5.332 ± 0.009	5.653 ± 0.013
Extinction Ratio min/max	0.0013 ± 0.0003	0.0008 ± 0.0003

Table 3.1: **Measurement results for V_π and the extinction ratio of the EOM's:** Both EOM's feature an extinction ratio in the order of 10^{-3} and a π -Voltage in the order of 5-6 V. This is compatible with the voltage range of the Pulsemaster that will drive the EOMs.

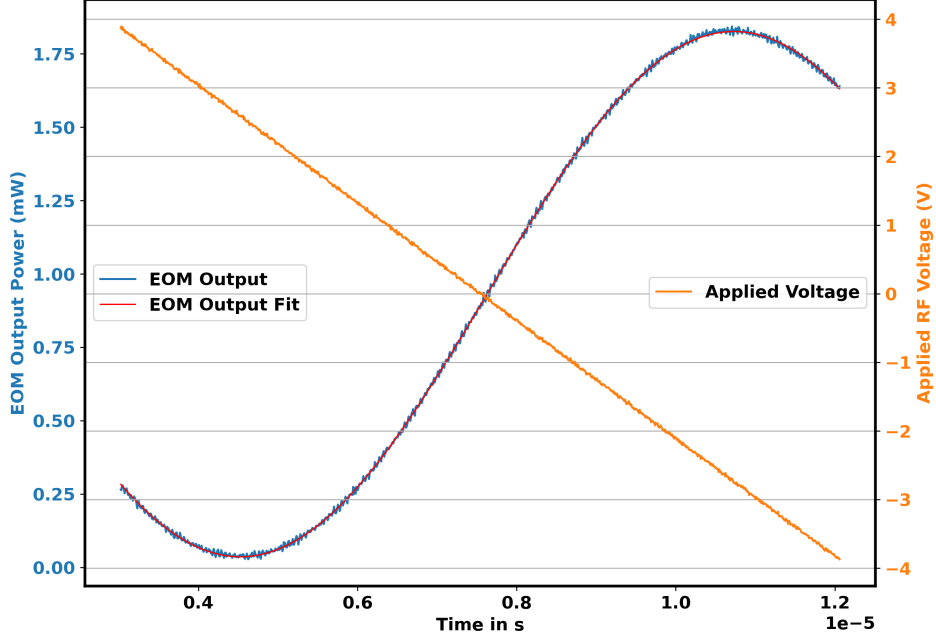


Figure 3.7: **Pi-Voltage Measurement:** Orange: The applied voltage at the RF port of the EOM. Blue: The resulting optical intensity change of the EOM output. By extracting the optical power minima and maxima from a fit and comparing it to the applied voltage difference, one finds V_π of the EOM. The extinction ratio of the EOM follows from comparing the minimum to the maximum optical output power.

Extinction Ratio of the AOM

By using an additional AOM in front of an EOM the aim is to improve the limited extinction ratio of the EOM. The overall possible extinction ratio is then the product of each respectively. Since very low powers close to zero need to be measured for P_{low} , the measurement is split into two parts, a low optical power measurement to find P_{high} and a high optical power one with additional attenuation of the AOM drive signal for P_{low} . The latter is then refactored by the increase in optical power c (Figure 3.8).

An on/off power protocol was recorded using the on/off switch command of the Urukul module with an off-time of 0.6 ms. For recording P_{high} (AOM drive on), the attenuation of the AOM driving signal was set low to 5.0 dB in ARTIQ. This results in maximum diffraction efficiency and thus higher optical throughput. The optical input power is set to 7.0 ± 0.2 mW. To measure P_{low} (AOM drive off), the optical power before the AOM was increased to 700 ± 2 mW and the attenuation in ARTIQ set to 31.0 dB. The measured power minimum is then refactored by the increase of optical power $c = 100$. 200 such ratios were measured and the mean and its deviation were calculated. The

final acquired maximum extinction ratio of the AOM is $R_{ext} = (8.46 \pm 0.07) \cdot 10^{-4}$. Together with the extinction ratio of the EOM, this leads to a decrease of the optical power from maximum to the minimum at full modulation depth of $R_{ext}(1.1 \pm 0.3) \cdot 10^{-6}$. This doesn't fulfill the benchmark of $R_{ext} \leq 3 \cdot 10^{-9}$.

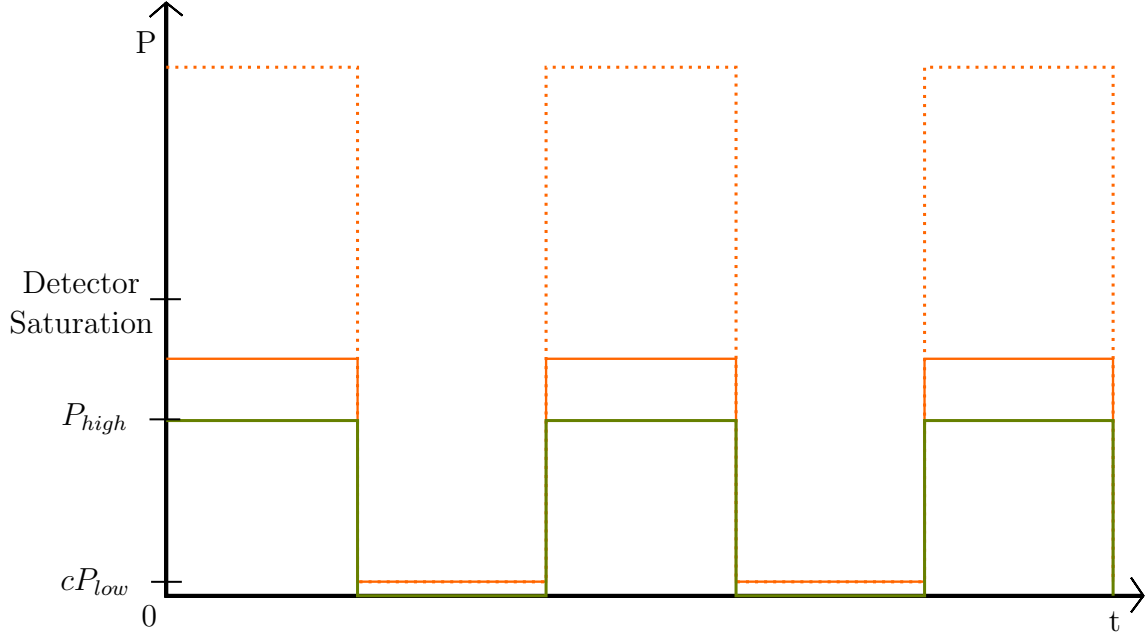


Figure 3.8: **AOM Extinction Ratio Measurement:** Green: Low optical input power but maximum modulation depth of the AOM. The mean of the top level is P_{high} . Orange: High optical input power but less modulation depth to stay within the detector's range. The dashed line illustrates the higher optical power which would saturate the detector for full modulation depth. The now higher power minimum, which is the mean of the lower level, is refactored by the increase of optical power to get P_{low} before calculating the extinction P_{low}/P_{high} .

For $\omega_0 = 2\pi \cdot 100$ kHz with a relative deviation of $\Delta\omega_0/\omega_0 = 5 \cdot 10^{-2}$ as measured in later chapters, this is equal to 0.9 ± 0.2 oscillations for $t_m = 1.34$ ms. For $\omega_4 = 2\pi \cdot 10$ kHz and assuming the same deviation, this equals 0.09 ± 0.02 oscillations for $t_m = 1.34$ ms. For $\omega_{2,3} = 2.5$ kHz we find 0.022 ± 0.006 oscillations for $t_m = 1.34$ ms. For $t_f = 0.66$ ms, it is reduced by a factor of 2.

The extinction ratio of the AOM can still be improved. The attenuation for the measurement of P_{high} is kept at 5.0 dB since at this power the Mini-Circuits ZHL-2W-1+ amplifier already reaches its maximum input power and starts to saturate. The diffraction efficiency for this driving power was measured to be 73 ± 2 % with a Thorlabs optical power sensor. Using a Moglabs Agile RF synthesizer with higher driving power, the diffraction efficiency was measured to be 88 ± 2 %. This increase of 21 ± 4 % for

P_{high} would decrease the extinction ratio by $21 \pm 8 \%$ which is not sufficient to reach the benchmarks for all beam lines. We conclude that while for $\omega_{2,3}$ the extinction ratio fulfills the benchmark of $\omega_{ff}t_{f,m} < 0.05$, it will require an improvement of 0.28 ± 0.08 for ω_4 and $(2.7 \pm 0.7) \cdot 10^{-3}$ for ω_0 in regard to R_{ext} . A possibility for lowering the extinction ratio further without adding an additional modulator would be to use the AOM in a double-pass configuration as in [40].

3.3.2 Characterization of the Pulse Performance

Deviation of the Initial Trapping and Cooling Frequency

We measure the deviation on the initial trapping frequency ω_0 by recording pulses at optical powers in the order of 10^2 mW as in [29]. Attenuation in the form of density filters avoids saturation or damage to the detector. We estimate that the results of the measurement are applicable to lower powers as well as reasoned in Section 3.3.1. Since the necessary cooling time is in the order of a few ms [18], 3 ms pulses are evaluated. The pulses were characterized for an AOM, second for an EOM, and third for the combination of both.

	Power P in mW	ΔP_n
AOM only	319.9 ± 0.6	$(4.85 \pm 0.06) \cdot 10^{-3}$
EOM only	201.0 ± 0.4	$(4.85 \pm 0.06) \cdot 10^{-3}$
AOM+EOM	195.1 ± 0.5	$(5.83 \pm 0.07) \cdot 10^{-3}$

Table 3.2: **Power Fluctuations of High Power Pulses:** We find the relative uncertainty ΔP_n as a measure for the width of the pulse power to have no significant impact on ΔP . For the combination of AOM+EOM we find a $\Delta\omega_0 = (5.1 \pm 1.7) \cdot 10^{-2}$.

We evaluated samples of 100 pulses over a period of 15 s at 14-bit resolution and a sampling rate of 62.5 MS/s (Table 3.2). The mean of the power for all modulators during the last 10 oscillations, representative of an initial trapping frequency ω_0 of the protocol, fluctuates by a relative uncertainty $\Delta P/P < 3 \cdot 10^{-3}$ for all modulators. For the combination AOM+EOM we find $\Delta P/P = (2.6 \pm 0.3) \cdot 10^{-3}$. This corresponds to a $\Delta\omega_0/\omega_0 = (5.1 \pm 1.7) \cdot 10^{-2}$ and is close to the benchmark of $\Delta\omega_0/\omega_0 = 5 \cdot 10^{-2}$. The width of the power for a single pulse during the last 10 oscillations is for all modulators at $\Delta P_n < 6 \cdot 10^{-3}$. This is so small that it doesn't have a significant effect on $\Delta\omega_0/\omega_0$

in the error propagation. The corresponding power distribution shows a Gaussian form (Figure 3.9).

As a measurement of rise- and fall times of the pulses in the next section shows (Table 3.3), the falling edge of an AOM+EOM makes up $\omega_0 t_{fall} = 0.0084 \pm 0.0001$ oscillations of ω_0 . This has no significant impact on $\Delta\omega_0/\omega_0$.

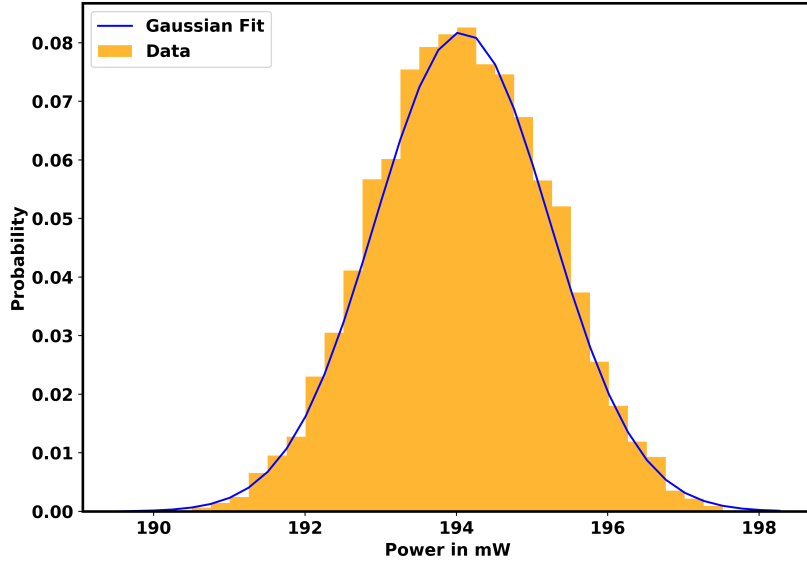


Figure 3.9: **Distribution of the Pulse Power:** This is the power distribution during the last 10 oscillations for $\omega_0 = 2\pi \cdot 100$ kHz of a single long AOM+EOM pulse. It shows a Gaussian form with $\mu = 194.1$ mW and $\sigma = 1.1$ mW.

Timing Precision

ARTIQ has an internal timing resolution down to units of 1 ns. Thus when programming a protocol, the actions are executed with nanosecond timing. Whether this is also true for the control of the proposed electronics and the optical modulators remains to be shown. The measurements in this chapter have been done with the internal measurement functions of a Teledyne LeCroy Wavepro 760-ZI oscilloscope at a sampling rate of 40 GS/s. This enables a resolution down to 25 ps and is thus sufficiently fast to resolve t_{width} and t_{rise}/t_{fall} .

The first measurement, described in Figure 3.10, shows that the mean pulse length of both the EOM with ± 0.03 ns as well as the AOM with ± 0.05 ns follow the ARTIQ

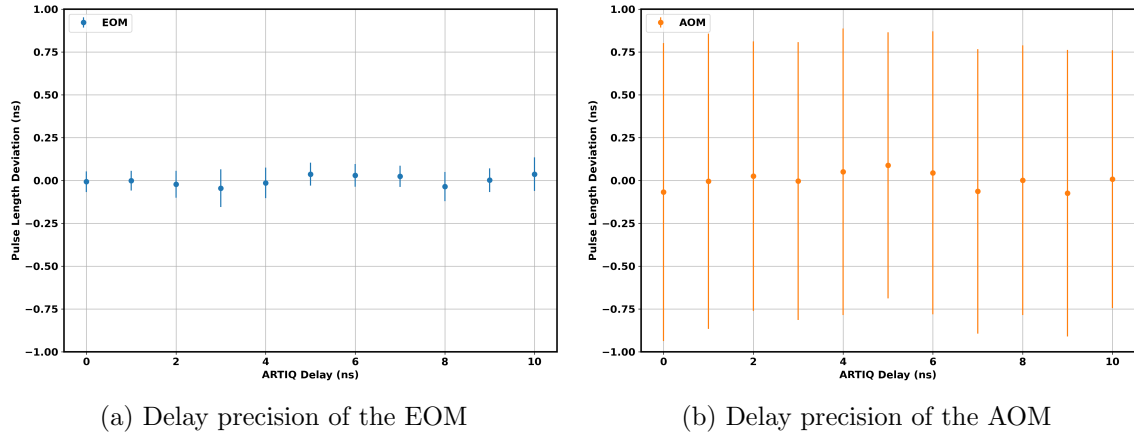


Figure 3.10: **Precision of the Modulator Response to ARTIQ Delays:** The measurements show that the mean pulse width of the optical signal of both a) the EOM at ± 0.03 ns and b) the AOM at ± 0.05 ns follow the time delay in ARTIQ at its smallest time unit of 1 ns. This implies that time durations in the light field protocol can be adjusted in 1 ns steps as desired.

delay in steps of 1 ns. A bias drift of the EOM can influence the pulse length when using the 50 % definition. This is because the bias drift causes a change in peak height and shifts the 50 % point in time since the TTL control of the Sinara is independent of the EOM. For the duration of ≈ 10 min of the above measurement, this was not relevant. For longer times, however, it might become relevant. The remaining deviations could either be caused by deviations in the measurement of the Sinara or by very small bias drifts. The much higher imprecision of the AOM pulses is possibly caused by fluctuations of the rise/fall of the internal RF switch of Urukul and thus the electronic drive or by an irregular response of the crystal. On average, however, the mean is almost as close to its target as for the EOM. Both Urukul for the AOM as well as the DIO-SMA module for the EOM are controlled by the same FPGA carrier and are synchronized to the same clock. Since nanosecond timing is possible for both the AOM and the EOM, it is in principle also possible for the combination of both.

Furthermore, measurements on the pulse performance were done, also specifically for the combination of an AOM and an EOM. This includes a measurement of the pulse length precision, rise- and fall times of the edges for 10 % / 90 % of the pulse maximum, and a measurement of the precision of space between pulses, corresponding to free expansions. The latter measurement is also done for separate EOMs to show that also for separate optical arms it is possible to achieve a similar precision (Figure 3.11).

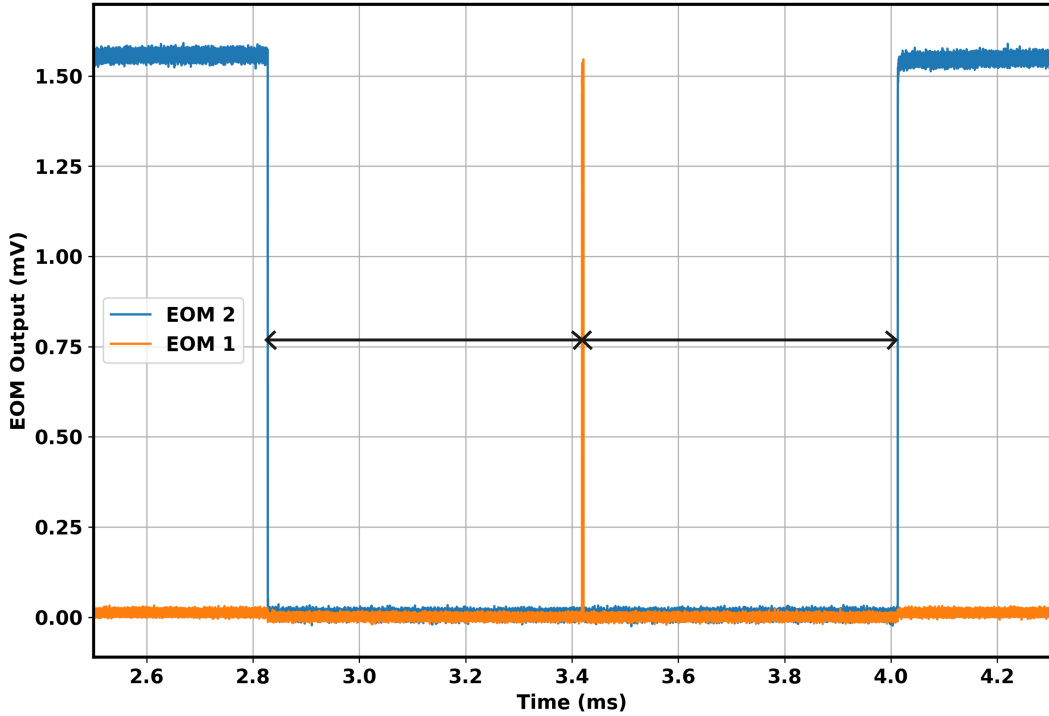


Figure 3.11: **Two Separate EOMs** : EOM 2 creates long 1 ms pulses while EOM 1 creates short $10 \mu s$ pulses. The timing precision between these pulses t_{space} is measured by looking at the distance between the two pulses at the 50 % level as indicated with black arrows. When taking a closer look, one sees that for this recording an AOM was placed in front of the EOMs. This is visible when looking at the edges of the zero-power parts as they are further lowered towards zero during off-times. As illustrated earlier in Figure 2.1 and 2.2 showing the planned experimental implementation, the pulses will be created by separate modulators in separate optical arms.

	AOM	EOM	AOM+EOM
Pulse Length (ns)	± 0.8	± 0.1	± 0.4
Rise (ns)	103.0 ± 0.8	17.4 ± 0.2	13.3 ± 0.2
Fall (ns)	95.0 ± 0.9	15.40 ± 0.15	12.2 ± 0.3
Pulse Space (ns)	± 0.8	± 0.1	± 0.4
For Separate EOM's (ns)	-	± 0.2	± 0.5

Table 3.3: **Characterization of the Pulse Timing Performance:** The EOM in general shows by far the fastest response and precision while the AOM is generally slower. The pulse space of separate EOMs (Figure 3.11) are timed almost as fast as pulses of a single EOM. All measurements show a $\Delta t < 1$ ns.

Since it has already been proven that the duration of the implied operations can be adjusted as desired, only the measured time precision is listed, except for rise- and fall times. All pulses and spaces were set with an ARTIQ delay of $10 \mu s$ to measure at the highest sampling rate of 40 GS/s. Recording longer pulses and pulse spaces at a delay

of $600 \mu s$ is restricted to 2.5 GS/s and the corresponding deviations showed to be restricted by the corresponding resolution. The results are given in Table 3.3. The EOM shows the fastest performance while the AOM is in general slower. All measurements yield a $\Delta t < 1 \text{ ns}$ and thus satisfy the goal of $\Delta t = 1 \text{ ns}$.

Area of the Pulse for the Nonlinearity

We measure the pulse area by integrating over the data points of short $10 \mu s$ pulses as proposed for the protocol. Assuming linearity of the power (see Section 3.3.1), higher powers up to 2 mW than the required $\approx 30 \mu W$ are used to exploit the full detector and oscilloscope range for maximum resolution on the relative uncertainty ΔA_{33} .

	AOM	EOM	AOM+EOM
$\Delta A_3/A_3$	$(9 \pm 1) \cdot 10^{-4}$	$(3.8 \pm 0.6) \cdot 10^{-3}$	$(2.2 \pm 0.7) \cdot 10^{-3}$
Normalized	$(7 \pm 2) \cdot 10^{-4}$	$(5.3 \pm 0.2) \cdot 10^{-4}$	$(1.6 \pm 0.6) \cdot 10^{-3}$
$\Delta P/P$	$(9 \pm 1) \cdot 10^{-4}$	$(3.8 \pm 0.6) \cdot 10^{-3}$	$(2.2 \pm 0.6) \cdot 10^{-3}$
Normalized	$(7 \pm 2) \cdot 10^{-4}$	$(5.3 \pm 0.2) \cdot 10^{-4}$	$(1.6 \pm 0.6) \cdot 10^{-3}$
Double Pulse	$(1.13 \pm 0.03) \cdot 10^{-4}$	$(3.1 \pm 1.6) \cdot 10^{-4}$	$(1.39 \pm 0.04) \cdot 10^{-4}$
Monitor	$(1.14 \pm 0.06) \cdot 10^{-4}$	$(4.2 \pm 0.5) \cdot 10^{-4}$	$(1.19 \pm 0.02) \cdot 10^{-4}$

Table 3.4: **Deviation of the Pulse Area:** The upper four lines show the relative uncertainties ΔA_3 and ΔP before and after normalization with the monitored power. While the normalization leads to an improvement, $\Delta A_3/A_3$ is still missing the benchmark of $\Delta A_3/A_3 \leq 0.7 \cdot 10^{-5}$ by a factor of $(4.4 \pm 1.6) \cdot 10^{-3}$ for AOM+EOM. The double pulse precision is evaluated by comparing the mean pulse area of the first and second pulse of a sample. The monitor does the same for the mean power during the time of the pulses. Considering the deviations, no difference is visible.

To be able to measure the precision of the benchmark $\Delta A_3/A_3 \leq 0.7 \cdot 10^{-5}$, it is necessary to have a measurement device of sufficient resolution. The measurements were taken at 15-bit vertical resolution and a sampling rate of 125 MS/s . This enables a relative vertical resolution of $6 \cdot 10^{-5}$ on the pulse height for a filled oscilloscope range and a horizontal resolution of $\Delta t = 16 \text{ ns}$ on the pulse length. Modeling the pulse as a square, the area of a $10 \mu s$ pulse filling the oscilloscope range can approximately be measured with a relative uncertainty of $\Delta A/A = 1.6 \cdot 10^{-3}$. This is calculated by Gaussian error propagation. It is dominated by the lack of horizontal resolution.

Since separate measurements were already done on the timing precision of such pulses, showing that the precision on the pulse length as well as the rise and fall behavior is in general $\Delta t < 1 \text{ ns}$, it is possible to infer a higher precision of the pulses. In this

order of timing, the theoretical bound of the square pulse approximation is lowered to at least $\Delta A/A = 1 \cdot 10^{-4}$.

Evaluating sets of 500 $10 \mu s$ pulses in a measurement of 15 s by integrating the data points shows that all modulators stay above this limit, where the AOM performs better than the EOM and the combination AOM+EOM (Table 3.4). A measurement of 1500 AOM pulses in 1 s indicates that there is a strong correlation of the pulse area with the pulse height with a Pearson's correlation coefficient of $r_P = 0.9996$ (Figure 3.12). In conclusion, the measurements were taken with additional monitoring of the optical input power to see whether incoming power fluctuations are the reason. This is done with the monitor arm for the AOM and the combination AOM+EOM as illustrated in Figure 3.1. For the EOM the light in the signal path is coupled into a 50:50 fiber BS where one output is connected to the EOM input and the other serves as the power monitor.

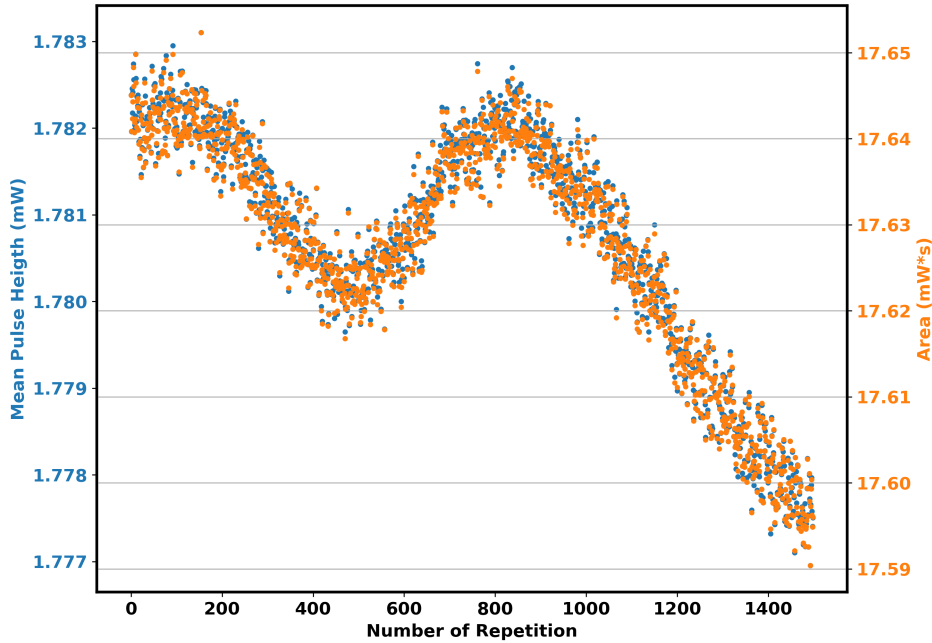


Figure 3.12: **Correlation of Pulse Height and Area:** Evaluating the height and area of 1500 short $10 \mu s$ pulses in about 1 s shows that the area is strongly correlated to the pulse height with a correlation of $r_P = 0.9996$. This suggests that optical power fluctuations are the main contributor to the deviation of the area.

After norming the pulse area and pulse height with the monitored input power to decouple the two effects, the precision improves, in the case of the EOM even by a full order of magnitude. Only for the AOM+EOM combination it stays above $\Delta A_3/A_3 = 1 \cdot 10^{-3}$. A possible reason is that while in this case, the monitor arm

can improve the power fluctuations as for the AOM, it is not able to counteract the fluctuations of the additional EOM as well as the fiber BS does.

Further study of the power monitoring shows that while for the EOM the monitoring with a 50:50 fiber BS very well correlates to the pulse signal with a correlation coefficient of $r_P = 0.997$ and improves the signal stability after normalization by $89 \pm 4 \%$, the monitoring with a separate coupler in the monitor arm performs much worse at a Pearson's coefficient of $r_P = 0.39$ and is less reliable at an average improvement of $32 \pm 17 \%$. The reason for the worse performance is found in a measurement comparing the fiber-detected optical power in the monitor arm to the signal arm, removing the modulators. Normalizing the signal arm to the monitor arm yields an improvement in the same order as with pulse modulation (Figure 3.13). A possible reason lies in the optical elements and the coupling into the fibers. Optimizing the coupling into the fibers with an additional telescope to adjust the beam size did not lead to an improvement. In opposite, the telescope introduced more coupling noise. This behavior suggests beam pointing instabilities.

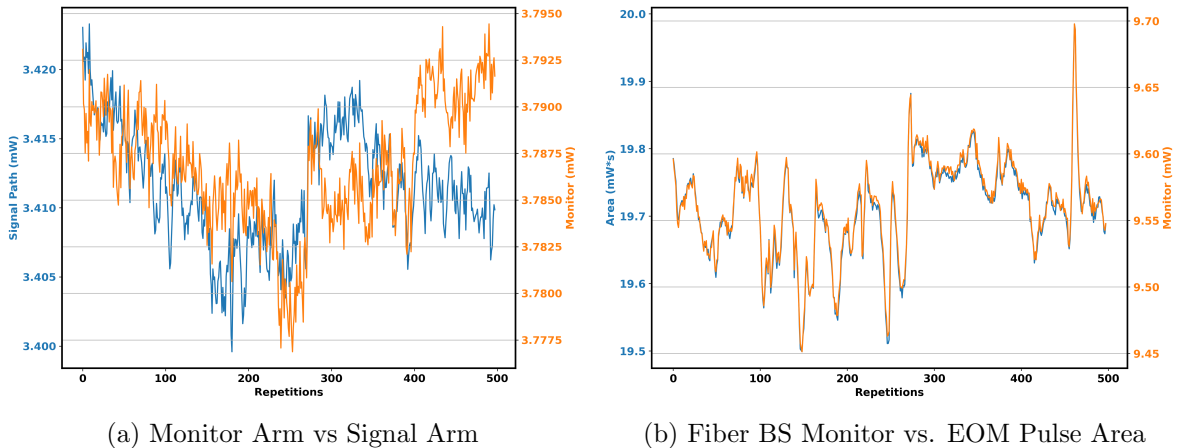


Figure 3.13: **Power Monitoring along 15 s:** a) Monitor Arm vs Signal Arm. The measurement shows that even without any modulator in the signal path the monitor arm does not very well correlate with the signal arm at a Pearson's coefficient of $r_P = 0.39$. This prevents an efficient normalization of the pulse power and suggests unstable optics with beam pointing issues. b) Fiber BS Monitor vs. Area. In comparison, monitoring the power for the EOM with a fiber BS results in a much better correlation with $r_P = 0.997$ is visible.

While fluctuations of the optical input power are one possible source of deviation in the pulse area, the modulators themselves and the electronic drive are another. To investigate whether there is an influence of the latter, the areas of $10 \mu s$ double-pulses

with short gaps of $5 \mu\text{s}$ are compared to each other to avoid the much slower input power fluctuations. The same is done with the monitor power during the time of these pulses. Higher fluctuations of the pulse areas compared to the monitored power would indicate additional noise coming from the modulation itself. The results are listed in the two bottom lines of Table 3.4.

As for the AOM and the combination of AOM+EOM, the pulse areas are about equal to each other within the same order as the monitor power and thus no relevant noise coming from electronics or the modulators is visible. The slightly higher error on the AOM+EOM pulses compared to the monitor arm might indicate some additional noise in the signal arm caused by the EOM, but a more likely explanation is the more sensitive PM fiber of the EOM. The EOM with the fiber BS monitor shows much higher fluctuations in general. Still, the precision of the pulse areas and the monitor overlap, indicating that also here no electronic/modulator noise is visible. Comparing the EOM and the AOM+EOM measurement further indicates that more stability is reached when directly coupling into the PM fiber of the EOM instead of butt coupling with a mating sleeve from the single-mode fiber BS output.

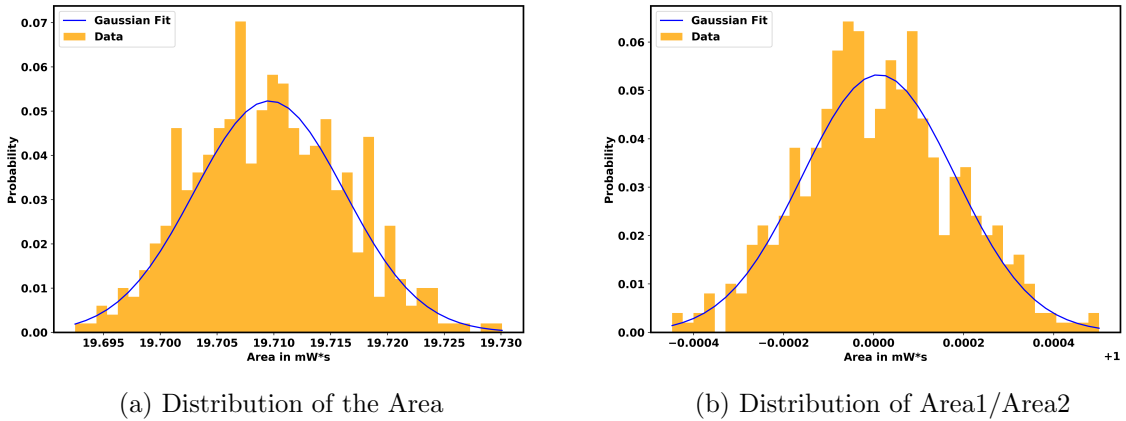


Figure 3.14: **Pulse Area Distributions:** Histograms of the data on the pulse area along ≈ 15 s show a gaussian normal distribution. a) Distribution of the pulse area of $10 \mu\text{s}$ pulses with $\mu = 19.7$ mWs and $\sigma = 0.007$ mWs. The pulses are created by an EOM and normalized with the monitored input power. b) Distribution of the precision on Area1/Area2 of $10 \mu\text{s}$ double-pulses with a $5 \mu\text{s}$ gap created by an EOM with $\mu = 1.00001$ and $\sigma = 0.00017$.

In conclusion, the relative precision on the pulse area for AOM+EOM does so far not meet the necessary benchmark by a factor of $(3 \pm 1) \cdot 10^{-3}$. The data shows that

the main contributor to the pulse area fluctuations in the current setup is fluctuations in power. While some part originates from coupling issues that might be caused by beam pointing and non-ideal optical elements, the intensity of the laser source itself contributes to the fluctuations as well. Normalizing the pulse area to the monitored input power does lead to an improvement of $\Delta A_3/A_3$, especially for the EOM where the power is monitored with a fiber BS. Furthermore, investigating double-pulses with short gaps and thus avoiding power fluctuations to some degree shows that the pulse area does in general fluctuate in the same order as the monitored input power. This proves that to the degree of the resolvable precision in the measurement, noise from the electronic drive or the modulators themselves is not visible.

It will be required for future investigations to have a more precise, possibly direct measurement device for the pulse area. When the necessary measurement precision is provided, investigations on feedback mechanisms for stabilizing the energy of the pulses will have to be done. The conclusion we can draw from this data is, however, that power stability is the main limiting factor for achieving the benchmark, and would require further active stabilization. Possible solutions for improving power stability are provided in [41, 42].

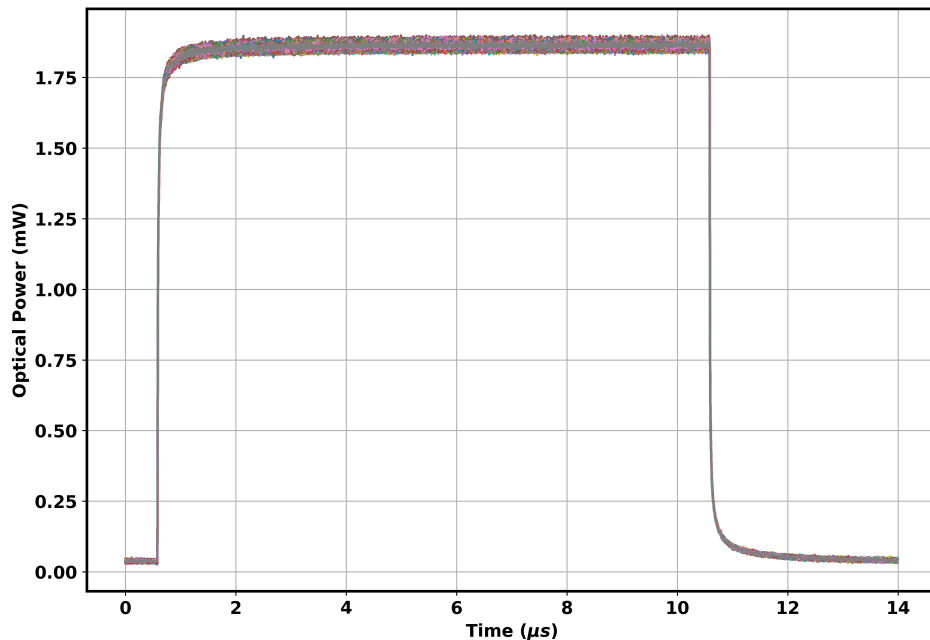


Figure 3.15: **Exemplary Short Pulse:** This graph exemplary shows 10 μs pulses created by an AOM for illustration of the pulse shape and edges. 150 recordings over a time of about 15 s were taken for this plot.

Precision of the Exponential Inflation Pulse

Measurements of 150 90 μs pulses in 15 s show that the earlier defined precision of $\Delta(\omega_4 t_4)/(\omega_4 t_4) \leq 3 \cdot 10^{-3}$ is not achieved (Table 3.5). While the timing of the pulses is already characterized in Section 3.3.2, we use the measurements only to find the power fluctuations. While the timing would allow reaching the benchmark, the current deviation is dominated by fluctuations in power. A power stabilization technique reducing the fluctuations by a factor of $(2.5 \pm 0.3) \cdot 10^{-3}$, similar to the nonlinearity, is required.

	AOM	EOM	AOM+EOM
P in mW	1.660 ± 0.003	1.231 ± 0.004	1.405 ± 0.006
$\Delta(\omega_4 t_4)$	$(4.2 \pm 1.4) \cdot 10^{-2}$	$(5.7 \pm 1.7) \cdot 10^{-2}$	$(6 \pm 2) \cdot 10^{-2}$

Table 3.5: **Results for the Exponential Inflation:** The relative uncertainty $\Delta(\omega_4 t_4)$ is limited by power fluctuations. It will require a relative improvement of power stability of $(2.5 \pm 0.3) \cdot 10^{-3}$ in order to reach the benchmark of $\Delta(\omega_4 t_4)/(\omega_4 t_4) \leq 3 \cdot 10^{-3}$

3.3.3 Discussion of the Measurement Results

The proposed experimental setup for controlling the light field in terms of the earlier defined protocol yet only partly meets the necessary benchmarks set in Section 2.2.2 for a successful reconstruction of the fringe pattern. The measurement results compared to the goals are displayed in 3.6.

	Target	Result
R_{ext}	$\leq 3 \cdot 10^{-9}$	$(1.1 \pm 0.3) \cdot 10^{-6}$
$\Delta\omega_0/\omega_0$	$\leq 5 \cdot 10^{-2}$	$(5.1 \pm 1.7) \cdot 10^{-2}$
$\Delta t_{f,m}$	$\leq \pm 1$ ns	$< \pm 1$ ns
$\Delta A_3/A_3$	$\leq 0.7 \cdot 10^{-5}$	$(2.2 \pm 0.7) \cdot 10^{-3}$
$\Delta(\omega_4 t_4)/(\omega_4 t_4)$	$\leq 3 \cdot 10^{-3}$	$(6 \pm 2) \cdot 10^{-2}$

Table 3.6: **Measurement Results:** Comparing the measurement results to the defined goals in section 2.2.2 shows that only $\Delta t_{f,m}$ and $\Delta\omega_0/\omega_0$ satisfy the required benchmarks. The extinction ratio R_{ext} will have to be improved by a factor of 0.28 ± 0.08 for ω_4 and $(2.7 \pm 0.7) \cdot 10^{-3}$ for ω_0 . The Area $\Delta A_3/A_3$ will need an improvement of $(3 \pm 1) \cdot 10^{-3}$ and $\Delta(\omega_4 t_4)/(\omega_4 t_4)$ will require a relative improvement of $(2.5 \pm 0.3) \cdot 10^{-3}$, both in regard to power stability.

A single EOM doesn't show a sufficient extinction ratio. However, measurements of

both an AOM and EOM in combination show that the extinction ratio will still require an improvement of $(2.7 \pm 0.7) \cdot 10^{-3}$ for the trapping beam at $\omega_0 = 2\pi \cdot 100$ kHz and an improvement of 0.28 ± 0.08 for $\omega_4 = 2\pi \cdot 10$ kHz.

The measurements on the initial trapping and cooling power show that the combination of an AOM+EOM satisfies the benchmark with $\Delta\omega_0/\omega_0 = (5.1 \pm 1.7) \cdot 10^{-2}$. For the timing of the pulses, it was shown that the resulting optical pulses can be adjusted at the resolution limit of 1 ns of ARTIQ. Both the pulse length and space between pulses show a precision below 1 ns and thus meet the goal of $\Delta t_{f,m} \leq 1$ ns. The AOM is slower in the rise and fall of its pulse edges and also less precise in timing compared to the EOM.

The pulse area does not meet the defined benchmark of $\Delta A_3/A_3 \leq 0.7 \cdot 10^{-5}$. The combination of AOM+EOM performs on average at $\Delta A_3/A_3 = (2.2 \pm 0.7) \cdot 10^{-3}$. Thus it will require an improvement of a factor $(3 \pm 1) \cdot 10^{-3}$. The measurements showed that the main limiting factor is fluctuations in power. At the available measurement precision, neither electronic noise in the driving signal nor noise from the modulator themselves is visible, but fluctuations of the laser power. Similarly, the benchmark of a relative $\Delta(\omega_4 t_4) \leq 1 \cdot 10^{-3}$ was not met with power fluctuations as the limiting factor. It will require an improvement by a factor of $(2.5 \pm 0.3) \cdot 10^{-3}$ to meet the defined goal.

3.4 Conclusion and Outlook

We presented an experimental realization of a protocol aiming to prepare a non-Gaussian quantum state with an interferometric standing wave scheme and light pulses. Necessary for the implementation of the light-field protocol, we suggested a realization of the electronic control for realizing such a protocol with light modulation using the Sinara hardware and ARTIQ software as the core system. This included:

1. **A study of the benchmarks of the relevant parameters of the electronic and optic control:** Based on possible noise and deviations of realistic optical pulses, we investigated how this affects the parameters of the protocol. The benchmarks were chosen such that the effect of deviations of the parameters are assumed to be negligible in regards to the deviation of the energy of the short non-linearity as the most sensitive part of the protocol. This retains the standard

deviation of the fringe spacing below 20 %, keeping the expected non-Gaussian fringe-pattern intact.

2. **We experimentally investigated to what extent the benchmarks are fulfilled in a test setup:** The electronic control fulfills our demands in regards to the timing of the pulses. However, the main limiting factor currently is deviations in the energy of the non-linearity, mainly caused by fluctuations in laser power, requiring an improvement of $(3 \pm 1) \cdot 10^{-3}$. The exponential inflation will require improvement on power fluctuations in a similar order of $(2.5 \pm 0.3) \cdot 10^{-3}$. This will need power stabilization and can be achieved with feedback mechanisms as in [41, 42]. Also, the extinction ratio of the modulators will require an improvement of $(2.7 \pm 0.7) \cdot 10^{-3}$. A possible solution would be to use a double-pass configuration as in [40].

The next steps toward the implementation of our method will be to characterize the possible extinction ratio when using the AOMs in a double-pass configuration. Furthermore, requiring the main focus to ensure the protocol works will be to develop a stabilization technique for the energy of the non-linearity. This will include the development of a reliable measurement device enabling a measurement precision of the pulse energy on the order of 10^{-6} . This will enable the necessary insight into any possible roadblocks for achieving a relative precision $\leq 0.7 \cdot 10^{-5}$ for the pulse area, also in regards to possible electronic noise not yet visible. It may be necessary to design a sufficient power stabilization technique. Furthermore, the control of the electric field will have to be implemented in the system.

Once the current roadblocks are solved, the fast control of optical potentials is successfully conquered. The proposed method can then be implemented in the setup, promising the nonlinear optical control of a wavepacket of a particle with $\approx 10^8$ amu mass.

Bibliography

- [1] P. S. Epstein, *Centennial of the Undulatory Theory of Light*, Science, Vol 63, Issue 1633, pp. 387-393 (1926) DOI: 10.1126/science.63.1633.387
- [2] A. Einstein, *Über einen die Erzeugung und Verwandlung des Lichtes betreffenden heuristischen Gesichtspunkt*, Annalen der Physik, 17 (6): 132–148 (1905) DOI: 10.1002/andp.19053220607
- [3] M. Planck, *Ueber das Gesetz der Energieverteilung im Normalspectrum*, Annalen der Physik, 4 (3): 553 (1901) DOI: 10.1002/andp.19013090310
- [4] L. V. de Broglie, *On the Theory of Quanta*, Ph.D. thesis (1924)
- [5] L.V. de Broglie, *The wave nature of the electron*, Nobel Lecture (November 1929)
- [6] G. P. Thomson and A. Reid, *Diffraction of Cathode Rays by a Thin Film*, Nature volume 119, page 890 (1927)
- [7] C. J. Davisson and L. H. Germer, *Reflection of Electrons by a Crystal of Nickel*, pages 317–322 (1928)
- [8] D. W. Keith, C. R. Ekstrom, Q. A. Turchette, and D. E. Pritchard, *An Interferometer for Atoms*, Physical Review Letters, 66(21):2693–2697 (1991)
- [9] M. Kasevich and S. Chu, *Atomic Interferometry Using Stimulated Raman Transitions*, Physical Review Letters, 67(2):2–5 (1991)
- [10] M. Arndt, O. Nairz, J. Vos-andreae, C. Keller, G. V. D. Zouw and A. Zeilinger, *Wave-Particle Duality of C 60 Molecules*, Nature, 401:680–682 (1999)

- [11] Y. Y. Fein, P. Geyer, P. Zwick, F. Kiałka, S. Pedalino, M. Mayor, S. Gerlich and M. Arndt, *Quantum Superposition of Molecules Beyond 25 kDa*, Nature Physics, 15 (12):1242–1245 (2019), DOI: 10.1038/s41567-019-0663-9
- [12] M. Arndt and K. Hornberger, *Testing the limits of quantum mechanical superpositions*, Nature Physics Vol. 10, pp 271–277 (2014)
- [13] S. Nimmrichter, *Macroscopic Matter-wave Interferometry*, Dissertation, University of Vienna (2013)
- [14] O. Romero-Isart, A. C. Pflanzer, F. Blaser, R. Kaltenbaek, N. Kiesel, M. Aspelmeyer and J. I. Cirac, *Large Quantum Superpositions and Interference of Massive Nanometer-Sized Objects*, PRL, 107(2):2–5 (2011), DOI: 10.1103/PhysRevLett.107.020405
- [15] J. Bateman, S. Nimmrichter, K. Hornberger and H. Ulbricht, *Near-Field Interferometry of a Free-Falling Nanoparticle from a Point-Like Source*, Nature Communications, 5:1–5 (2014), DOI: 10.1038/ncomms5788
- [16] O. Romero-Isart, *Coherent Inflation for Large Quantum Superpositions of Levitated Microspheres*, New Journal of Physics, 19(12):1–5 (2017), DOI: 10.1088/1367-2630/aa99bf
- [17] R. Kaltenbaek, G. Hechenblaikner, N. Kiesel, O. Romero-Isart, K. C. Schwab, U. Johann and M. Aspelmeyer, *Macroscopic Quantum Resonators (MAQRO): Testing Quantum and Gravitational Physics with Massive Mechanical Resonators*, Experimental Astronomy, 34(2):123–164 (2012), DOI: 10.1007/s10686-012-9292-3
- [18] L. Neumeier, M. A. Ciampini, O. Romero-Isart, M. Aspelmeyer, N. Kiesel, *Fast Quantum Interference of a Nanoparticle via Optical Potential Control*, Publication in Preparation (2022)
- [19] L. Neumeier, *Private Communication*
- [20] L. Magrini, P. Rosenzweig, C. Bach, A. Deutschmann-Olek, S. G. Hofer, S. Hong, N. Kiesel, A. Kugi and M. Aspelmeyer, *Real-time Optimal Quantum Control of Mechanical Motion at Room Temperature*, Nature vol. 595, 373–377 (2021)

- [21] L. Magrini, P. Rosenzweig, C. Bach, A. Deutschmann-Olek, S. G. Hofer, S. Hong, N. Kiesel, A. Kugi and M. Aspelmeyer, *Real-time optimal quantum control of mechanical motion at room temperature*, URL: <http://arxiv.org/abs/2012.15188> (2021)
- [22] U. Delić, M. Reisenbauer, K. Dare, D. Grass, V. Vuletić, N. Kiesel, and M. Aspelmeyer, *Cooling of a Levitated Nanoparticle to the Motional Quantum Ground State*, *Science*, 367(6480):892–895 (2020), DOI: 10.1126/science.aba3993
- [23] F. Tebbenjohanns, M. L. Mattana, M. Rossi, M. Frimmer and L. Novotny, *Quantum Control of a Nanoparticle Optically Levitated in Cryogenic Free Space*, *Nature* vol. 595, 378–382 (2021), DOI: 10.3929/ethz-b-000480147
- [24] David J. Griffiths, *Quantenmechanik*, Pearson Verlag, 2nd Edition (2012)
- [25] Markus Aspelmeyer, Tobias J. Kippenberg, Florian Marquardt, *Cavity Optomechanics*, *Rev. Mod. Phys.* 86, 1391 (2014)
- [26] Nikolai Kiesel, Florian Blaser, Uroš Delic, David Grass, Rainer Kaltenbaek, and Markus Aspelmeyer, *Cavity cooling of an optically levitated submicron particle*, *PNAS*, Vol. 110, No. 35, 14180–14185 (2013)
- [27] D. Grass, *Levitated optomechanics in vacuum using hollow-core photonic crystal fibers and optical cavities*, Ph.D. Thesis (2018)
- [28] L. Novotny and B. Hecht, *Principles of Nano-Optics*, Cambridge University Press, 1st Edition (2006)
- [29] S. Lindner, *Towards optical levitation of nanoparticles below 10^{-9} mbar*, Master Thesis, University of Vienna (2021)
- [30] J. Rieser, *Towards Optical Levitation in UHV: Loading using Hollow-Core Photonic Crystal Fibers*, Master Thesis, University of Vienna (2020)
- [31] C. Bach, *Detection of a levitated particle’s mechanical motion close to the Heisenberg limit*, Master Thesis, University of Vienna (2021)
- [32] M. Reisenbauer, *Dissipative Optomechanics on a Levitated Microresonator*, Master Thesis, University of Vienna (2018)

- [33] D. Friedrich et al, *Laser interferometry with translucent and absorbing mechanical oscillators*, New J. Phys. 13 093017 (2011)
- [34] D.E. Chang, C.A. Regal, S.B. Papp, D.J. Wilson, J. Ye, O.J. Painter, H.J. Kimble, and P. Zoller, *Cavity optomechanics using an optically levitated nanosphere*, PNAS, vol. 107, No. 3, 1005–1010 (2010)
- [35] iXblue Photonics, *Introduction to iXBlue Mach-Zehnder Modulators Bias Controllers*, URL: <https://www.ixblue.com/wp-content/uploads/2021/12/introduction-to-ixblue-mbc-2019.pdf> (7.06.2022)
- [36] *Sinara Open Hardware Project*, URL: <https://github.com/sinara-hw> (7.06.2022)
- [37] *ARTIQ Github*, URL: <https://github.com/m-labs/artiq> (7.06.2022)
- [38] *ARTIQ Documentation*, URL: <https://m-labs.hk/artiq/manual/> (7.06.2022)
- [39] Valley, George E., Jr., Wallman, Henry, *Vacuum Tube Amplifiers*, MIT Radiation Laboratory Series, vol. 18, p. 73 (1948)
- [40] W. J. Schwenger and J. M. Higbie, *High-speed acousto-optic shutter with no optical frequency shift*, Rev. Sci. Instrum. 83, 083110 (2012), DOI: 10.1063/1.4746292
- [41] F. Tricot, D. H. Phung, M. Lours, S. Guerandel, and E. de Clercq, *Power stabilization of a diode laser with an acousto-optic modulator*, Review of Scientific Instruments 89, 113112 (2018) DOI: 10.1063/1.5046852
- [42] J. Phrompao, R. Pongvuthithum, T. Sucharitakul, K. Srakaew, and W. Anukool, *Real-time and versatile laser-power stabilization with arbitrary amplitude modulation*, J. Phys.: Conf. Ser. 1380 012034 (2019)
- [43] M. A. Nielsen and I. L. Chuang, *Quantum Computation and Quantum Information*, Cambridge University Press, 7th press (2019)